

Document downloaded from:

<http://hdl.handle.net/10251/183205>

This paper must be cited as:

García-Oliver, JM.; Niki, Y.; Rajasegar, R.; Novella Rosa, R.; Gómez-Soriano, J.; Martínez-Hernández, PJ.; Li, Z.... (2021). An experimental and one-dimensional modeling analysis of turbulent gas ejection in pre-chamber engines. *Fuel*. 299:1-15.
<https://doi.org/10.1016/j.fuel.2021.120861>



The final publication is available at

<https://doi.org/10.1016/j.fuel.2021.120861>

Copyright Elsevier

Additional Information

An experimental and one-dimensional modeling analysis of turbulent gas ejection in pre-chamber engines

J.M. García-Oliver^a, Y. Niki^b, R. Rajasegar^c, R. Novella^a, J. Gomez-Soriano^a,
P. J. Martínez-Hernández^a, Z. Li^c, M.P.B. Musculus^c

^aCMT – Motores Térmicos, Universitat Politècnica de València, Camino de Vera, 46022 Valencia, Spain

^bNational Institute of Maritime, Port and Aviation Technology, Tokyo, 181-0004, Japan

^cSandia National Laboratories, Livermore, CA, United States

Abstract

Experimental results from a study on the evolution of gas jets ejected through the orifices of a pre-chamber in a heavy-duty optical engine are presented. The work examines conditions without fuel inside the main-chamber, which helps to describe the dynamics of the ejected gas jets without the interference of subsequent combustion in the main-chamber. Experimental diagnostics consist of high-speed visible intensified imaging and low-speed infrared imaging. Additionally a one-dimensional gas jet model is used to characterize the spatial distribution of the ejected flow, including parameters such as tip penetration, which are then validated based on experimental results. Different stages in the ejection of pre-chamber jets are identified, with chemical activity restricted to a maximum distance of 5 to 10 orifice diameters downstream of the orifice as indicated by the recorded visible radiation. Sensitivity of cycle-to-cycle variations in pre-chamber jet development to the air-to-fuel ratio in the pre-chamber observed in the experiments is in most part attributed to the variations in the timing of combustion initiation in the pre-chamber. The influence of the ejection flow on the penetration of the gas jet on a cycle-to-cycle basis is presented using the one-dimensional model. The one-dimensional model also indicates that the local flow exhibits highest sensitivity to operating conditions during the start of ejection until the timing when maximum flow is attained. Differences that exist during the decreasing mass-flow ejection time-period tend to smear out in part due to the transient slowdown of the ejection process.

Keywords: *Pre-chamber spark ignition, 1-D gas jet model, cycle-to-cycle variability, infrared imaging, high-speed visualization*

*Corresponding author.
email: jgarciao@mot.upv.es

1. Introduction, motivation and objectives

In the search for higher thermal efficiency and lower fuel consumption in internal combustion engines, pre-chamber spark-ignition system is leading a new chapter in the improvement of spark-ignition engines' performance. The considerable increase in scientific publications related to this technology over the past few years demonstrates the appreciable growth in both scientific and commercial interests in pre-chamber spark-ignition systems. Many researchers have documented the main advantages of pre-chamber spark-ignition systems for use in high-power stationary power plants [1, 2] and in transport applications [3, 4, 5, 6] through several engine experiments. Under suitable operating conditions, pre-chamber spark-ignition guarantees extremely low cycle-to-cycle variation (CCV) and an accelerated combustion process [7], which minimizes knocking due to end-gas auto-ignition compared to conventional spark-ignition systems [8, 9, 10, 11], and thus allows for an increase in the compression ratio that can further improve engine thermal efficiency [12]. In addition, its active version, with a dedicated fuel injector inside the pre-chamber, allows to increase the dilution limit to extremely lean mixtures ($\lambda \sim 2.5$), while reducing nitrogen oxides (NO_x) emissions to near zero levels [7, 13].

Despite the general benefits of this ignition system being well established, the fundamental aspects of turbulent jet-based ignition are not fully understood, which hinders a complete concept optimization that in turn limits its market penetration [14]. For example, currently, there is no consensus on the combustion regimes that are encountered during the ejection of the gases from the pre-chamber at engine-relevant conditions involving ultra-lean mixtures.

To shed some light on this aspect, several researchers have utilized different visualization techniques applied to simplified devices such as divided constant-volume chambers and rapid compression machines (RCM). In a pioneering work [15] the visualization of pre-chamber ignition process in a divided chamber bomb through high-speed schlieren imaging and OH^* radiation was performed. Different ignition patterns were identified when modifying the nozzle diameter and the equivalence ratio in the main chamber. More recently, several experiments in a similar device using simultaneous high-speed schlieren [16] and OH^* chemiluminescence imaging [17] were carried out to describe the jet penetration and ignition process. A relationship between the Damköhler number and the combustion regime in the main-chamber was established using semi-empirical correlations.

29 The temporal evolution of the ejected pre-chamber jets was related to the ignition kernel develop-
30 ment within the pre-chamber in [18, 19] using experimental visualizations and numerical simulation
31 in a simplified pre-chamber apparatus at ambient pressure. The measurements showed the influence of
32 the jet dynamic structure and mixture composition on the main-chamber ignition process. In particular,
33 the authors emphasized on the importance of jet penetration length, jet duration, and reaction zone
34 presence in the performance of this system.

35 The lack of fundamental analyses of the characteristics of premixed turbulent jets under engine-
36 relevant conditions motivated other research works based on RCM optical measurements. In [20] and
37 [21], the influence of nozzle diameter and equivalence ratio on jet morphology and ignition location in
38 a radially mounted single hole pre-chamber was studied. Similarly, pre-chamber spark-ignition systems
39 were compared in [22] with conventional systems using both high-speed OH* imaging and integrated
40 UV emissions using a photomultiplier in an axially assembled four-nozzle pre-chamber that allowed for
41 visualization of interaction between the reacting jets.

42 Despite some attempts involving studies based on real engine architecture to characterize the im-
43 pact of the pre-chamber spark-ignition systems on the engine cycle-to-cycle variability, the root causes
44 of this phenomenon have not been analyzed in detail due to facility limitations [23]. The complexity
45 of applying visualization techniques in internal combustion engines due to the limited optical access
46 increases significantly when considering a small dead volume (pre-chamber) connected by small ori-
47 fices. Indeed, in small engines, it is practically impossible even to include a pressure transducer inside
48 the pre-chamber. In this sense, there is an important dearth of knowledge related to the fundamentals
49 of cycle-to-cycle variability in pre-chamber spark-ignited engines. Only the work in [24] delves into
50 one of the possible root causes of CCV. They studied the asymmetries in the jet dynamics and structure
51 of the pre-chamber jets (jet-to-jet variation) using numerical methods. Jet-to-jet variations were at-
52 tributed to the asymmetric formation of the initial spark kernel inside the pre-chamber, which resulted
53 in asymmetrical distribution of the turbulent jets actuated from six different orifices.

54 In the context of numerical simulations, a large number of investigations have been performed in
55 parallel to the previously discussed experiments. Starting from simplistic simulations based on un-
56 steady Reynolds Averaged Navier-Stokes (URANS) formulation [25, 26, 27, 28] to more sophisticated
57 ones such as Large-Eddy Simulations (LES) [29, 19, 30] and even Direct Numerical Simulations (DNS)
58 [31, 32, 33], multiple researchers have addressed different aspects of the pre-chamber combustion

59 process including the filling process, local flow distribution, flame quenching through the nozzle and
60 the associated composition field. However, it is not easy to establish a direct and quantitative con-
61 nection based upon such highly sophisticated calculation tools between pre-chamber combustion and
62 the resulting characteristics of the ejected gas jet, which is essentially central for the prediction of the
63 combustion process in the main-chamber. The development of simplified models accounting for the
64 fundamental physics of pre-chamber gas jet ejection and the associated combustion process is an area
65 where contributions are rather scarce. Few examples are available, such as the one in [18], where a
66 two-zone model was developed to predict the time evolution of conditions inside the pre-chamber up
67 to the nozzle. However, no link to the ejected gas jet structure was established. In terms of simplified
68 tools, one-dimensional (1-D) models have been successfully utilized for analysis of diesel-type sprays,
69 thereby coupling low computational costs and high prediction capabilities. Especially when boundary
70 conditions are highly controlled, they can deliver an accurate prediction of tip penetration and overall
71 mixing behavior [34, 35, 36]. Most of the assumptions used to develop these models are based on
72 turbulent gas jet theory [37]. For example, one of the core simplifications is that the radial spread of
73 axial momentum and mass fraction of the injected stream are self-similar, which reduces the flow to a
74 quasi-steady 1-D problem. Therefore, pre-chamber gas jets are good candidates for the application of
75 these diesel-type spray models. To the best of the authors' knowledge, no direct application of such an
76 approach has been reported in the literature. The availability of such tools with low computational cost
77 would help to bridge the gap between the pre-chamber combustion process and the associated gas jet
78 ejection, which would eventually contribute to a more efficient optimization of this concept for engine
79 applications [23, 38, 39].

80 In the present work, pre-chamber spark-ignited engine experiments are conducted in a single-
81 cylinder, heavy-duty, optical engine to characterize the development of turbulent jets and to discuss
82 the role of the ejected flow in the subsequent ignition of the main-chamber mixture. To this end, fuel is
83 only injected in the pre-chamber i.e., no main-chamber fueling is performed, so that the development
84 of the turbulent pre-chamber gas jets into an air ambient can be analyzed without the interference of
85 combustion in the main-chamber. Although some of the previously cited investigations have applied
86 this method with pre-chamber jets ejecting into the main-chamber without any fuel, they only use it
87 as a reference case for the later analysis of a realistic fueling case in the engine, without performing
88 a detailed analysis of the jet dynamics under realistic engine conditions. Cycle-to-cycle and jet-to-jet

89 variations will be the predominant focus of this work. In this study, experimental analysis is supported
 90 using a 1-D jet model, which is validated and applied for evaluation of cycle-to-cycle variability in tip
 91 penetration. Boundary conditions for the 1-D jet model in terms of mass-flow rate at the nozzle and
 92 in-cylinder conditions are estimated based on closed-cycle engine models, including both pre-chamber
 93 and main chamber. Both experimental and modeling efforts contribute to the understanding of the
 94 relevant phenomena during the pre-chamber ejection process.

95 **2. Experimental methods**

96 *2.1. Optical engine and operating conditions*

97 Experiments are performed in a single-cylinder, heavy-duty optical engine. Visualization is carried
 98 out through a Bowditch-type piston with an open, right-cylindrical bowl fitted with a flat fused silica
 99 piston-crown window (Figure 1). The major specifications of the engine are summarized in Table 1,
 100 with further details about the facility available elsewhere [40].

Table 1: Major specifications of the single-cylinder optical engine.

Engine base type	Cummins N-14, DI diesel
Displacement [L]	2.34
Bore x Stroke [cm]	13.97 x 15.24
Base compression ratio [-]	11.2
Combustion chamber	Quiescent, direct injection
Bowl Width x Depth [cm]	9.78 x 1.55
Swirl ratio [-]	0.5

101 Although originally developed as a heavy-duty, optically accessible, single-cylinder diesel engine, it
 102 has been suitably modified to operate as a gas engine. The engine is fitted with a pre-chamber spark-
 103 ignition module located centrally in the cylinder. The pre-chamber has a volume of 4.66 ml, with 8
 104 equally spaced, 1.6 mm diameter orifices machined with an included angle of 130°. The pre-chamber
 105 tip protrudes 10.6 mm below the fire deck. The pre-chamber houses a Rimfire Z1 spark plug and a
 106 Bosch HDEV5 GDI injector with 6 unequally spaced, 0.17 mm diameter orifices (Figure 1). A synthetic
 107 mixture comprising 95%CH₄, 4%C₂H₆ and 1%C₃H₈ by volume is used as a surrogate for natural gas.

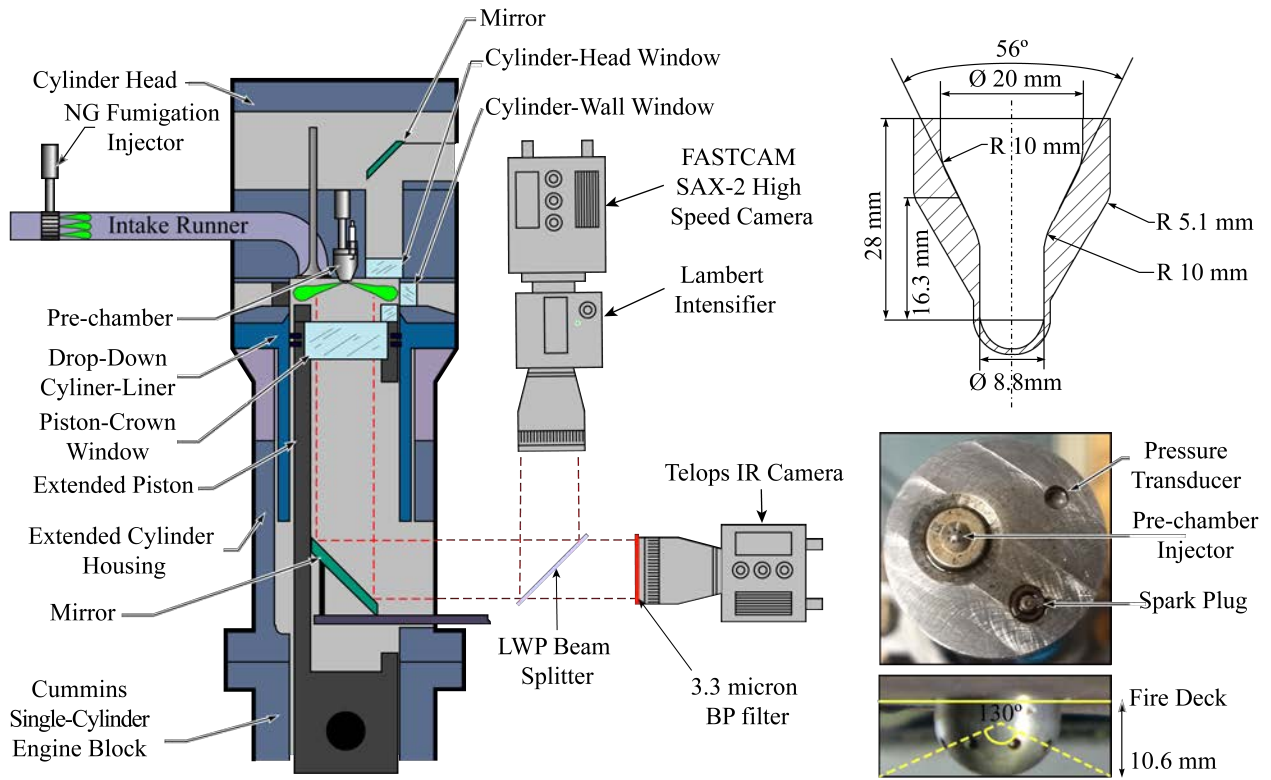


Figure 1: Schematic layout of the (a) optical engine and imaging setup (b) internal geometry of the pre-chamber (c) pre-chamber spark ignition system and its components as installed in the optical engine.

108 According to the objective of the study, no fuel is injected at the intake manifold, so that the ejection
 109 of pre-chamber jets into an air-ambient can be investigated. The engine is operated at 1200 rpm with
 110 constant intake conditions (105 kPa and 41°C) such that nominal bulk air conditions of 19 bar and
 111 730 K are reached at a spark timing of 343 CAD (crank angle degree), which is maintained constant.
 112 A sweep of air-fuel ratio (λ) in the pre-chamber (Table 2) has been performed by varying the start and
 113 duration of pre-chamber injector energization, so that a constant timing of 336.6 CAD for the end of
 114 solenoid energization (6.4 CAD before spark timing) is maintained. Injection pressure is kept constant
 115 at 100 bar throughout the study. Air-fuel ratio values in the table have been calculated by considering
 116 the air mass contained in the pre-chamber at spark timing and the total injected fuel mass, since no
 117 fuel leakages into the main-chamber can be expected before combustion-induced gas ejection.

118 The optical engine is operated in a 9 : 1 skip-fire mode, i.e. nine motored cycles precede each fired
 119 cycle, which minimizes the amount of residual gases present inside the pre-chamber and the main-
 120 chamber clearance volume. This allows for a fundamental study governing the ejection of pre-chamber
 121 gas jets avoiding any residual gas effects. Each experimental test run consists of 30 fire cycles after the
 122 engine is motored for 60 seconds at constant speed.

Table 2: Operating conditions as defined by a λ sweep in the pre-chamber along with the corresponding injected fuel mass.

λ	Fuel mass [mg]
1.65	1.56
1.50	1.72
1.25	2.06
1.07	2.41
0.94	2.76
0.83	3.10
0.75	3.45

123 2.2. Experimental diagnostics

124 Diagnostics include time-resolved pressure measurements both in the pre-chamber and the main-
 125 chamber along with imaging of broadband luminosity in the visible and infrared region. Figure 1 shows
 126 the schematic layout of the optical engine fitted with the pre-chamber spark ignition system along with
 127 the imaging setups.

128 Main-chamber pressure P_{MC} and pre-chamber pressure P_{PC} are measured using an AVL QC34D
 129 piezoelectric pressure transducer and an uncooled KISTLER PiezoStar piezoelectric pressure transducer,
 130 respectively. Both pressure traces are recorded every quarter crank angle degree. For every fired cycle
 131 during which images are acquired, the pressure difference between pre-chamber and main-chamber
 132 ($\Delta P = P_{PC} - P_{MC}$) is used extensively for analysis. Furthermore, an apparent heat release rate is
 133 calculated based on the whole instantaneous in-cylinder volume, i.e. pre-chamber plus main-chamber
 134 [41]. This curve will be used as an input to the modeling approach described later.

135 Radiation from the main-chamber is imaged through the piston window using a beam splitter ar-
 136 rangement for a two-camera system:

- Broadband visible (VIS) radiation is imaged using a Photron FASTCAM SAX-2 high-speed camera equipped with a Lambert Hi-CATT high-speed intensifier with a S-20 photocathode. This setup records time-resolved images at a 0.5 CAD resolution with a projected pixel size of 7.5 *pix/mm*. The camera effective exposure time is setup by the intensifier gain, which is 50 μs . Due to the absence of soot in this type of combustion, VIS radiation primarily corresponds to chemiluminescence of products of the pre-chamber combustion being ejected into the main-chamber, or of those species recombining to final products in the main-chamber.
- Infrared (IR) radiation is imaged using a Telops Hyp4 camera equipped with a Spectrogon band-pass filter centered at 3.3 μm with a 215 *nm* full width at half-maximum. Due to slow acquisition speed of this camera, it can only acquire only one image per cycle, with a projected pixel size of 4.5 *pix/mm*. The camera exposure time is 15 μs . IR radiation is emitted due to the C – H vibrational stretching of hot unreacted fuel at elevated in-cylinder temperatures caused by compression and/or combustion, or due to the thermal radiation by the hot combustion products emitting VIS radiation.

Due to the difference in the temporal resolution between the two cameras, the experimental methodology has consisted of recording information from 30 fired cycles, for each of which a single IR image, a VIS image sequence and pre-chamber and main-chamber pressure traces are acquired. Image acquisition timing has been suitably adjusted such that every single IR image is simultaneous with one of the VIS images from the 30 acquired sequences. For that purpose, the engine shaft synchronization system has been programmed to send the trigger pulses to both cameras at the specified camera acquisition CAD timings. Figure 2 shows an example of the acquired information for one fired cycle: A single IR image from that particular cycle, 5 selected VIS snapshots from the recorded VIS sequence along with the corresponding ΔP signal and the penetration of the pre-chamber gas jets derived from both IR/VIS images. The latter information is obtained by processing the corresponding IR/VIS images using typical Diesel spray processing algorithms as detailed in [35]. Detected contours (colored outlines in Figure 2) have been overlaid onto the images to improve visualization. Maximum axial extent of the IR/VIS radiation measured from the orifice exit will be referred to as *IR penetration* and *VIS penetration* respectively. Only IR images show the maximum axial-extent (penetration) of the gas jet tip clearly,

165 while VIS images only show a radiation zone that is mostly limited to the near orifice region. Hence,
 166 the wording *gas jet penetration* is only appropriate for the IR-derived information. However, confusion
 167 will be avoided by using the corresponding IR/VIS acronym.

168 3. Modelling approach

169 As discussed earlier in the introduction, the aim of this work is to validate a modeling approach that
 170 speeds up the design process by predicting gas jet penetration, which has been found to be a governing
 171 parameter in pre-chamber combustion. This methodology combines two main tools, a 0-D engine model
 172 and a 1-D jet model. Compared to CFD approaches, the main advantage of combining these tools is the
 173 fast computation time, which leads to a reduction in the associated computation costs while ensuring
 174 a reasonable agreement with experimental results.

175 A schematic layout of the overall modelling workflow is presented in Figure 3. Inputs to the 0-D
 176 engine model are pressure and temperature at inlet valve closing (IVC), spark timing, injected fuel
 177 mass and apparent heat release rate (AHRR). Momentum flux and mass flow rate through the holes are

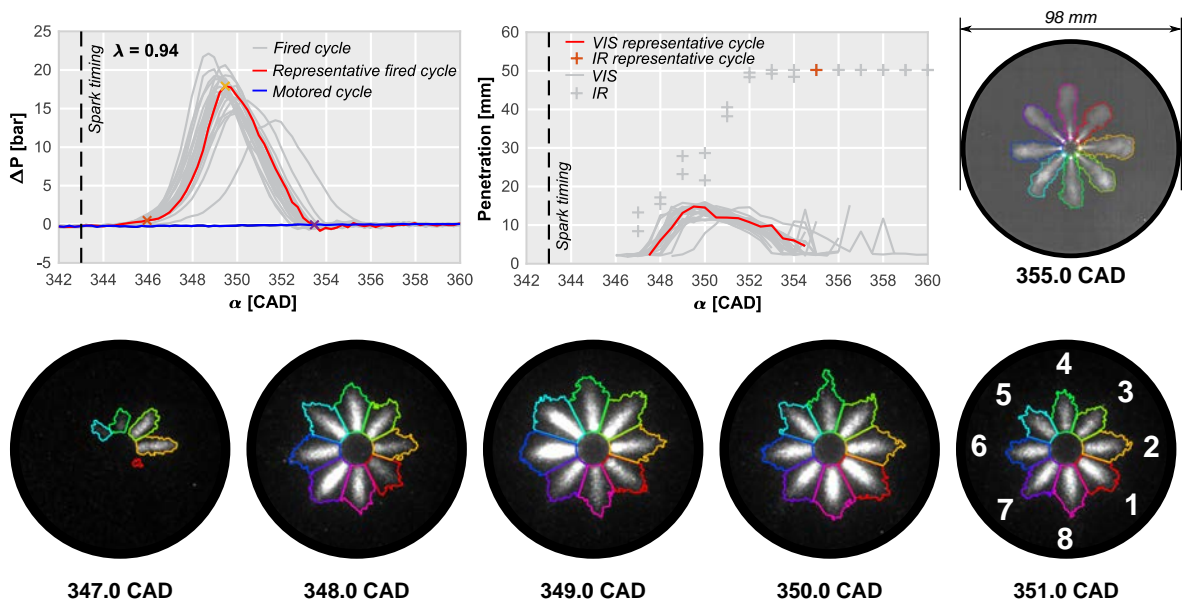


Figure 2: Sample of acquired and processed information from a single fired cycle for $\lambda = 0.93$. Top row: ΔP (left), IR- and VIS-penetration (middle) and IR image (right)), simultaneous with the VIS image acquired at 349 CAD. Bottom row: Sequence of five VIS images. Overlaid colour lines show detected contours from the image processing algorithm on the corresponding IR/VIS images.

178 obtained along with the thermodynamic conditions in the main-chamber from the engine modelling
 179 part. These results serve as the main inputs for the 1-D jet model, which predicts jet penetration for a
 180 single ejected gas jet (S). This modeling workflow can be used on a fully predictive basis, as proposed
 181 in [42] by using reasonable assumptions for the AHRR in the pre-chamber. However, the overarching
 182 goal of this work is the validation of the whole simulation workflow against experimental data. To this
 183 end, experimental AHRR is used as input, while the final predicted pre-chamber gas jet tip penetration
 184 profile is compared with the corresponding experimental values.



Figure 3: Schematic layout of the modeling workflow coupling a 0-D engine model with the 1-D gas jet model.

185 3.1. 0-D Engine model

186 The engine model is built up within the framework of a commercial 1-D engine modelling software
 187 (GT-Power) following the methodology from a previous work [23]. However, in the present case the
 188 approach has been simplified to consider only the closed-volume part of the engine cycle, where pre-
 189 chamber gas jet ejection and combustion occur. A submodel is implemented for the main-chamber and
 190 the pre-chamber, where they are both treated as engine cylinders connected through the pre-chamber
 191 orifices with the pre-chamber considered as a non-moving piston. This model reproduces the pressure
 192 evolution in both chambers along with the gas exchange between them based on the imposed heat-
 193 release rate profile.

194 Heat release profiles can be imposed either only on the pre-chamber or on the main-chamber, or
 195 on both of them. The experimental AHRR includes the combined effect of both chemical heat release
 196 and heat transfer in the whole main- and pre-chamber volume. However, because of the absence of
 197 fuel in the main chamber, the chemical part of AHRR should only be occurring in the pre-chamber.
 198 For the simulation part, the chemical part is the one to be imposed only in the pre-chamber. The
 199 reconstruction of this chemical part starting from the experimental one is performed in a simplified
 200 way, namely the experimental AHRR trace is properly scaled to deliver the fuel energy content in the
 201 pre-chamber (fuel mass times lower heating value). Other predictive approaches for the heat-release

rate are also feasible, but since the goal of this work is focused on the validation of the workflow, this quasi-diagnostics approach applied here is considered reasonable for our purposes, i.e., a quantitative description of the gas jet flow using the 1-D jet model.

Simulations are carried out into two different steps. The first one consists of a motored cycle, compressing air starting from IVC until the spark timing as set in the experiments. This is followed by a second simulation starting from the start of spark until the end of the cycle. In the second simulation, the fuel-air mass in the pre-chamber is initialized at pressure and temperatures values obtained at the end of the previous simulation. This defines the initial conditions on which the apparent heat-release rate profile is imposed to complete the remaining portion of the closed cycle.

Gas within the pre-chamber is modeled as a perfectly homogeneous mixture with a composition that evolves with time as combustion progresses in a single-zone fashion. Hence, the ejected pre-chamber flow is a mixture of air, fuel and burned products (CO_2 , H_2O and N_2), which is indeed a simplification of reality as confirmed by the experimental results. The composition of the burned products is set by considering complete stoichiometric combustion. The eight pre-chamber orifices are simulated using a combination of hole and pipe templates. The ejection velocity, mass flow rate and momentum flux from one of the eight orifices is then later used as input for the 1-D gas jet model.

The engine model is calibrated using the experimental data by varying the heat transfer and orifice discharge coefficients until there is reasonable agreement between the simulated and experimental pressure profiles in both the pre-chamber and main-chamber. An example of the calibration results for $\lambda = 0.94$, i.e., experimental (blue) and simulated (orange) pressure profiles is shown in Figure 4. The light blue area corresponds to the standard deviation in the experimental pressure profiles. Validation results indicate that the 0-D engine model is able to accurately reproduce the experimental pressure trends, thereby making it suitable for our analysis.

3.2. 1-D jet model

As discussed earlier in the introduction, one of the main objectives of this work is to validate this modeling approach for the prediction of ejected gas jet penetration. For this purpose, an existing 1-D jet model [36, 43, 44, 45] is adapted for this application. Although this 1-D jet model has been compared in the past with CFD RANS simulations of gas jets [36, 43], most of its applications have been Diesel-like sprays. A detailed description of this model can be found in [36, 43] so only the modifications carried out to simulate the gas jets for the pre-chamber configuration are described here:

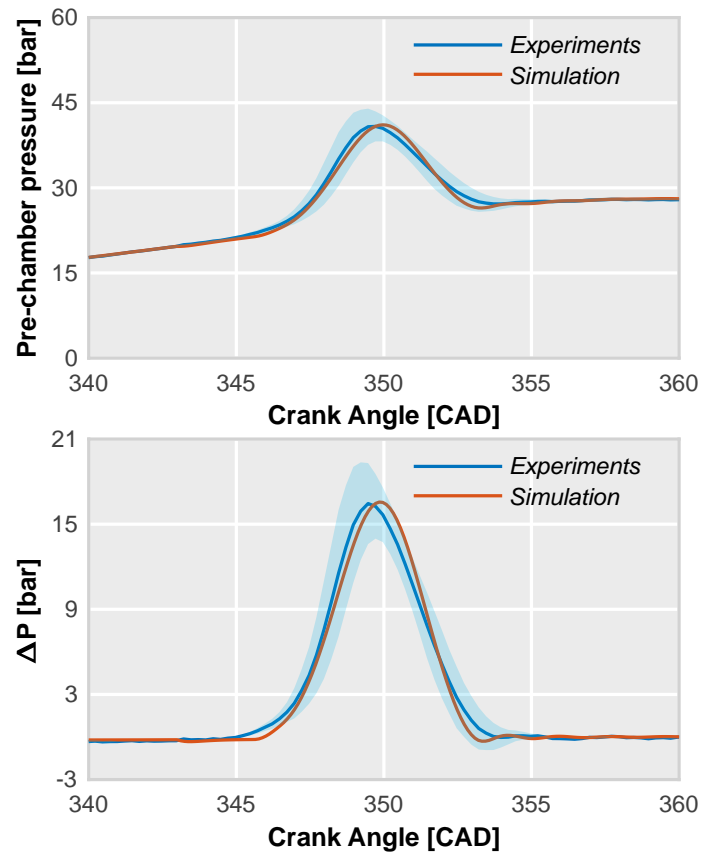


Figure 4: Left: Experimental and simulated pre-chamber pressure profile for $\lambda = 0.94$. Right: Pressure difference (ΔP) between the pre-chamber and main-chamber for the same operating condition.

- 232 • An inert configuration is analyzed in this work, i.e., the model describes the turbulent mixing of
 233 hot ejected pre-chamber gases with the air ambient in the main-chamber. Although VIS images
 234 show some radiation in the vicinity of the pre-chamber nozzle, most of the ejected gas jet volume
 235 shows no evidence of chemical activity further downstream of this region.
- 236 • The pre-chamber gas jets are modeled as a gas stream injected through the orifices from the pre-
 237 chamber into the main-chamber filled with air. Hence, an ideal gas equation of state is used, and
 238 a low Mach approach is assumed in terms of compressibility.

- 239 • Flow inputs to the 1-D jet model are the time evolution of mass and momentum fluxes through
240 the pre-chamber orifice, which are outputs obtained from the previously described 0-D engine
241 simulations. As opposed to the typical flat top-hat injection profiles used for diesel-like sprays,
242 evolution of such quantities for the pre-chamber configuration is found to be highly transient as
243 shown later.
- 244 • While in Diesel-like sprays a cold flow is injected in a hot environment, in this case a stream
245 of a high-temperature fluid (around 1500 K based on 0-D engine simulations) from the pre-
246 chamber is ejected into the main-chamber with the ambient at a relatively lower temperature
247 (700 K). Temperature and mixture composition at the pre-chamber orifice exit are assumed
248 to time-independent (constant) for the sake of simplicity. Since the focus of this work is on
249 penetration predictions, the most critical parameters are the nozzle momentum flux and ambient
250 density, which govern the jet dynamics. In the most simplified scenario, a non-reacting gas jet
251 could be considered as a constant-density flow [46]; thus, the role of orifice temperature and
252 mixture composition can be effectively ignored.
- 253 • Boundary conditions of the main-chamber into which the pre-chamber gas is ejected consists of a
254 time varying density and temperature profile that are also obtained from 0-D engine simulations.
- 255 • One of the critical parameters for the application of the 1-D jet model is the radial cone angle,
256 which is often used as a fitting parameter for the experimental tip-penetration data [35]. Here,
257 a constant cone angle of 25° is used. Modelled start of ejection has been shifted for all cases to
258 accommodate for the initial part of ejection process, which is highly challenging to capture in 1-D
259 models due to the uncertainties during the first instants of flow ejection.
- 260 • Although interaction between the pre-chamber gas jets and the piston-bowl wall are to be ex-
261 pected in experiments, the 1-D gas jet model only accounts for free-jet propagation.

262 Figure 5 shows the predicted ΔP and the momentum flux at the orifice as derived from the modelling
263 approach as an example of the coupling between the 0-D engine model and the 1-D gas jet one. Main-
264 chamber density is also included, as both momentum flux at the orifice and density of the ambient into
265 which ejection occurs govern the tip penetration of the pre-chamber gas jets, similar to Diesel sprays
266 [43]. Density in the main chamber during the main ejection period is roughly around 11.0–11.5 kg/m³

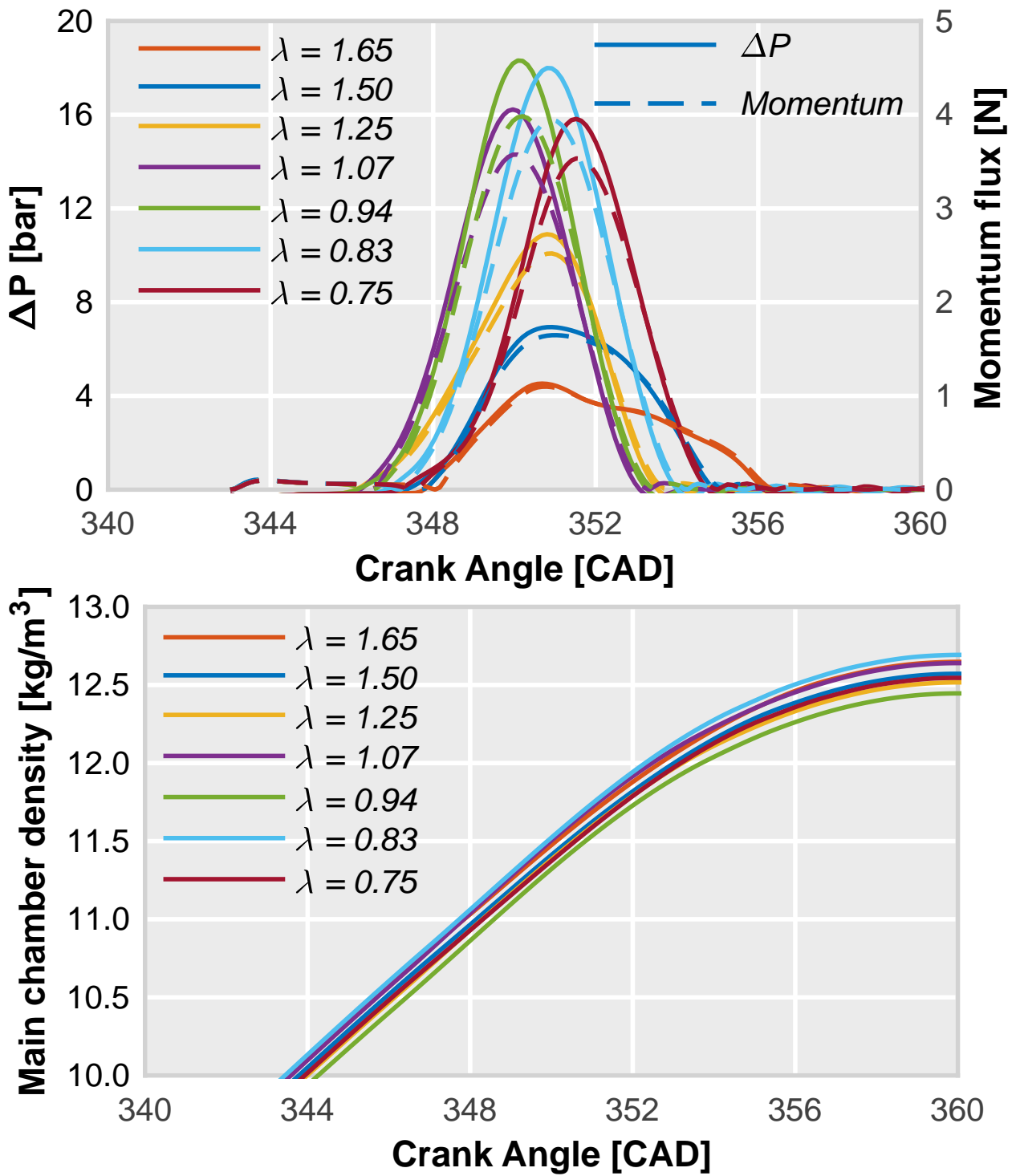


Figure 5: Left: Comparison of the modelled pressure difference ΔP (solid lines) and jet momentum (dashed lines) for various λ . Right: Evolution of main-chamber density for various λ .

267 for all conditions, as engine intake conditions are constant in this study. On the other hand, ΔP is an
268 indicator of the thermal state in the pre-chamber as a result of heat release and it is also the governing
269 parameter for the ejection velocity (and hence momentum) through the pre-chamber holes. Results will
270 evidence the strong relationship between both variables, and hence between pre-chamber combustion
271 and gas jet ejection. Momentum delivery starts when pre-chamber pressure increases as a result of
272 combustion to a value high enough to overcome the cylinder pressure and establish a flow through the
273 orifice. The expected proportionality in the time evolution between both variables (ΔP and momentum
274 flux) is observed, which also suggests the prominent role of pre-chamber pressure in gas jet ejection,
275 even though compressibility effects might play a role. In terms of λ sensitivity, the highest values of
276 peak ΔP are achieved under fuel-rich conditions ($\lambda = 0.94$), where pre-chamber combustion is fastest,
277 with peak ΔP values decreasing when moving away from these conditions, specially for the leanest
278 cases.

279 **4. Analysis of pre-chamber combustion cycle-to-cycle variation**

280 **4.1. Experimental assessment of cycle-to-cycle variation**

281 One of the most prominent features observed in this study has been the cycle-to-cycle variability in
282 the experiments. Figure 6 shows results that exemplify this phenomenon for $\lambda = 1.50, 0.94, 0.75$. The
283 results are from 30 individual fired cycles along with a *representative cycle* (highlighted in red) identified
284 based on the selection criteria discussed below. Both pressure difference ΔP between pre-chamber and
285 the main-chamber along with jet tip penetrations from both IR and VIS images are included. High
286 cycle-to-cycle variability is noticeable in all three metrics for both the lean ($\lambda = 1.5$) and rich cases
287 ($\lambda = 0.75$), while this is not so apparent for the near stoichiometric case ($\lambda = 0.94$). In terms of
288 pressure difference, variations influence both the timing of the initial rise, as well as the values of peak
289 ΔP attained. Variation in timing is also observable in the VIS-based penetration results with similar
290 peak values. As a single IR image is acquired every fired cycle, the cycle to cycle variation cannot be
291 described based upon IR images.

292 To normalize this timing variability, a so-called 'Start of Ejection' (SOE_p) is defined as the crankangle
293 position where the pressure increase (ΔP) exceeds 0.5 *bar*. Figure 7 presents the same results of
294 Figure 6 but on a SOE_p -referenced crankangle basis. From a qualitative perspective, it is clear that
295 the variation in ΔP decreases significantly especially for the rich case on this modified SOE_p -based

296 time referencing. Therefore, it is reasonable to infer that the timing of initial pressure rise within the
 297 pre-chamber is most likely to be a major source of the observed cycle-to-cycle variability. However, the
 298 overall shape of ΔP evolution, which dictates the apparent heat-release rate, remains similar. Using
 299 the new SOE_p -based time-reference also decreases the variations in both IR and VIS-based penetration.
 300 Even though cycle-to-cycle variability is lowest for stoichiometric conditions, some IR-based penetration
 301 measurements (350 CAD) are consistently off-trend compared to the adjacent timings. However, when
 302 plotted against a SOE_p -based crank angle scale, they tend to follow a single consistent trend. Similar
 303 to ΔP , all the VIS-based penetration traces are now in phase, with peak penetration values occurring
 304 close to the maximum ΔP timing. This minimization in cycle-to-cycle variation of ΔP and IR/VIS-based
 305 penetration evolution is very evident for the rich case. For the lean case, although the SOE_p -based crank
 306 angle reference removes the variation in IR/VIS-based penetration for the most part, some spread in
 307 the trends is still noticeable. Thus, the cycle-to-cycle variation observed in pre-chamber events for
 308 stoichiometric and rich conditions is mainly related to the fluctuations in the start timing of the ejection
 309 event. Otherwise, this remains repeatable in terms of both ΔP and IR/VIS-based penetration.

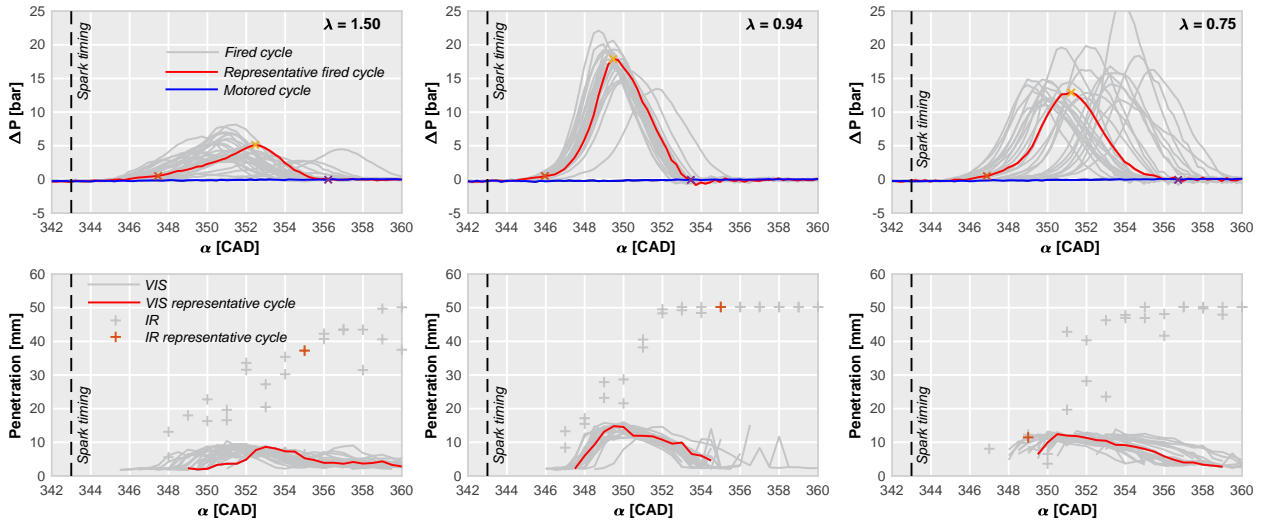


Figure 6: Pressure difference ΔP between pre-chamber and main-chamber (top) and jet tip penetration (bottom) based on IR (single markers) and VIS (lines) images. $\lambda = 1.50$ (left), 0.94 (middle) and 0.75 (right). Results are from 30 individual fired cycles (gray lines and markers) along with a representative cycle (highlighted in red) identified based on the selection criteria discussed in Section 4.1. Vertical dashed line corresponds to the timing of the spark.

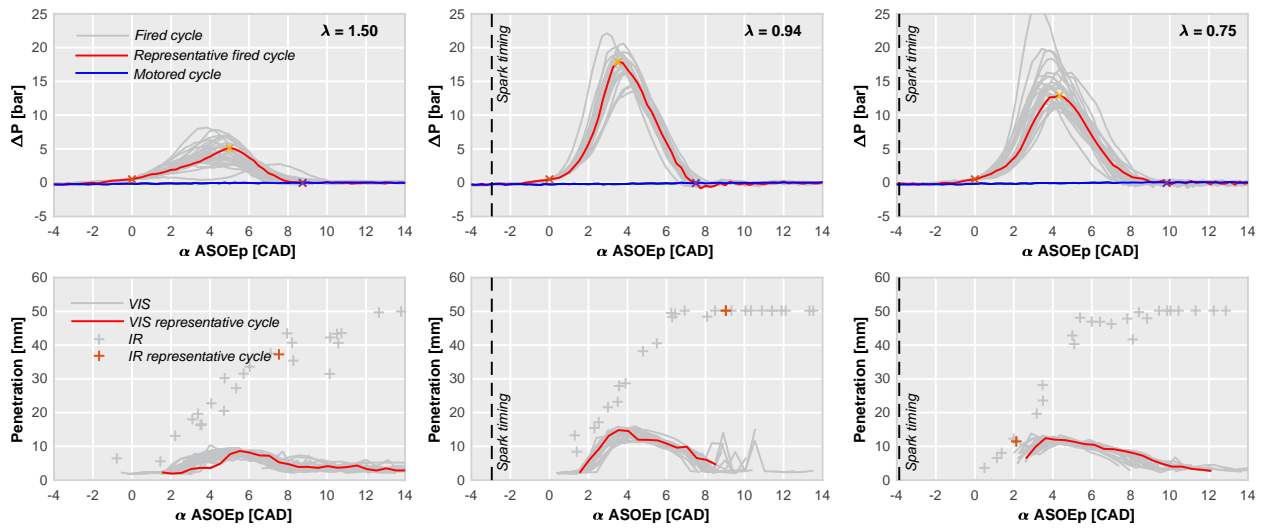


Figure 7: Pressure difference ΔP between pre-chamber and main-chamber (top) and jet tip penetration (bottom) based on IR (single markers) and VIS (lines) images. $\lambda = 1.50$ (left), 0.94 (middle) and 0.75 (right). Crank angle values are referenced to the start of ejection SOE_p , defined based on ΔP exceeding 0.5 bar. Results are from 30 individual fired cycles (gray lines and markers) along with a representative cycle (highlighted in red) identified based on the selection criteria discussed in Section 4.1. Vertical dashed line corresponds to the timing of the spark.

310 The earlier analysis revealed a strong link between the pressure difference and the timing of pre-
 311 chamber gas jet evolution on a cycle-to-cycle basis. To shed further light on this one-way dependence,
 312 Figure 8 compares the evolution of the start of ejection as derived from the pressure difference (SOE_p)
 313 to that from VIS images, now defined as the timing of VIS penetration exceeding 5 mm (SOE_{VIS}). The
 314 dependence of start of ejection (SOE_p and SOE_{VIS}) on λ is quite similar for both cases, with the start
 315 of ejection reaching minimum values around stoichiometry and increasing with rich and lean mixtures.
 316 Another characteristic crank angle position is also plotted in Figure 8, namely the timing of maximum
 317 pressure difference $\alpha_{\Delta P_{max}}$, which also exhibits a similar dependency with λ . Differences between these
 318 characteristic timings are almost constant, namely a 2.5° CA difference between the two start of ejection
 319 definitions and 1.0° CA difference between the start of ejection (SOE_{VIS}) and $\alpha_{\Delta P_{max}}$. This confirms
 320 a stable time sequence of pre-chamber events independent of λ : starting with the pressure rise in the
 321 pre-chamber, followed by the appearance of visible light caused by the ejection of active species and
 322 products of combustion from the pre-chamber, leading to maximum pressure difference between the
 323 pre-chamber and the main-chamber beyond which the combustion begins to recede.

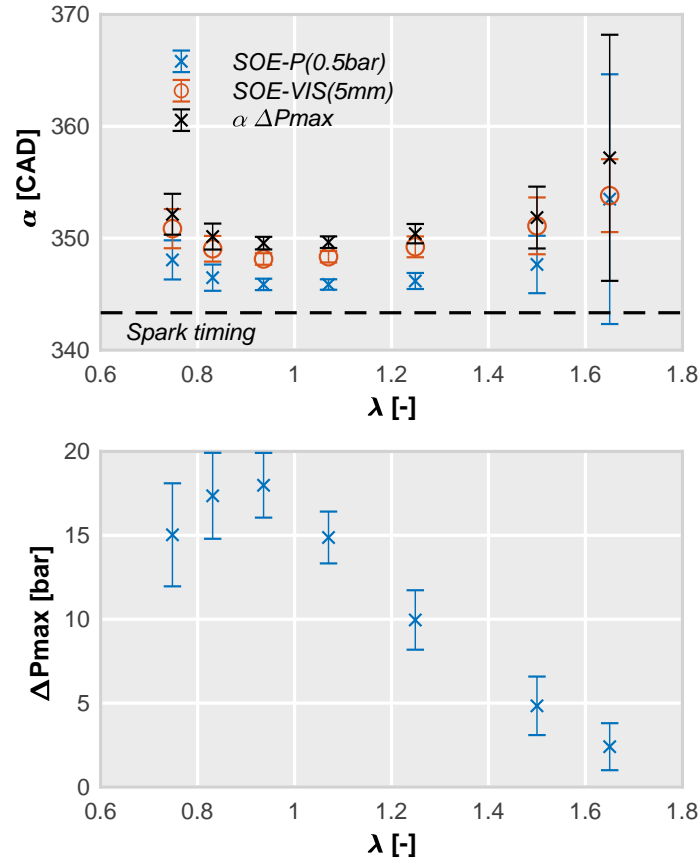


Figure 8: Start of ejection based on ΔP exceeding 0.5 bar (SOE_p) and VIS-based penetration exceeding 5 mm (SOE_{VIS}) and the timing of maximum ΔP (top) and maximum ΔP values (bottom) for various λ . Markers indicate the sample-averaged value with error bars corresponding to one standard deviation.

324 The peak pressure difference (ΔP_{max}) shown in Figure 8 can be considered as an indicator of the
 325 maximum heat release rate inside the pre-chamber during the combustion process. Compared to the
 326 timing evolution, the dependence of ΔP_{max} on λ appears to be reversed, with ΔP_{max} reaching highest
 327 levels at slightly rich conditions, consistent with laminar flame speeds peaking at slightly rich condi-
 328 tions. The magnitude of error bars on the start of ejection timing also indicate that the variation in
 329 combustion timing becomes significant at mixture compositions that deviate from stoichiometry. For
 330 ΔP_{max} , the absolute variation becomes more pronounced on the rich side, while the relative variation
 331 (i.e. the size of the error bar compared to average value) is especially large for lean mixtures. The main
 332 conclusion is that the combustion timing in the pre-chamber, the peak pressure difference (ΔP_{max}) and
 333 the subsequent ejection processes are strongly dependent on λ , with fastest and most stable combustion
 334 happening around stoichiometry.

335 Figure 9 shows the ΔP profile for individual fired cycles for the same three λ values (0.94, 1.5
336 and 0.75) as analyzed previously with four cycles highlighted: the ensemble-averaged cycle, the single
337 cycles with the maximum and minimum peak pressure difference (ΔP_{max}) and the most *representative*
338 cycle in the sample [47]. The *representative cycle* is defined as the individual cycle that most resembles
339 the average of the samples both in terms of combustion timing and peak pressure difference. In practice,
340 it is chosen as the one cycle that minimizes the merit function f in equation (1) amongst all cycles in the
341 sample. This merit function for a given j th cycle takes into account the maximum pressure difference
342 (ΔP_{max}) and three characteristic crank angle timings, namely the crank angle of maximum pressure
343 difference ($\alpha_{\Delta P_{max}}$), the start of combustion (α_{SoC}) and the end of combustion (α_{EoC}) as defined based
344 on the apparent heat-release rate. These variables for every firing cycle are compared against the
345 sample-averaged value of all cycles (denoted by the overbar in equation (1)).

$$f^j = \frac{|\Delta P_{max}^j - \overline{\Delta P}_{max}|}{\overline{\Delta P}_{max}} + \frac{|\alpha_{\Delta P_{max}}^j - \overline{\alpha}_{\Delta P_{max}}|}{\overline{\alpha}_{\Delta P_{max}}} + \frac{|\alpha_{SoC}^j - \overline{\alpha}_{SoC}|}{\overline{\alpha}_{SoC}} + \frac{|\alpha_{EoC}^j - \overline{\alpha}_{EoC}|}{\overline{\alpha}_{EoC}} \quad (1)$$

346 Though the results in Figure 9 indicate that the representative cycle is similar to the mean cycle
347 under stoichiometric conditions, where cycle-to-cycle variations remain low, the differences become
348 more evident at lean and rich mixtures. It is precisely this increased spread (dispersion) in the profiles
349 that results in an ensemble-averaged cycle that exhibits a much broader combustion duration with lower
350 ΔP_{max} values than most cycles in the sample and thereby is not considered representative of the typical
351 combustion evolution. For example, the ΔP_{max} value for the ensemble-averaged cycle for a rich mixture
352 ($\lambda = 0.75$) is lower than the cycle with minimum ΔP_{max} values. Thus, the representative cycle based
353 on the function of merit described in equation (1) is more appropriate than ensemble averaging to get a
354 realistic evolution of combustion. Corresponding ΔP profiles and VIS- and IR-based penetration values
355 for this representative cycle have been also highlighted in Figures 6 and 7.

356 4.2. 1-D modelling analysis of scattering

357 Since 1-D models usually rely on ensemble-averaged cycle results, they cannot take into account
358 the effect of cycle-to-cycle variability intrinsically. To overcome this caveat, an indirect evaluation of
359 jet tip penetration variability is obtained by running the model with different input values. As de-
360 scribed earlier in Section 3.1, the experimental heat release rate is an input parameter to the modeling
361 workflow, which is calculated based on the pressure evolution in the pre-chamber and main-chamber.

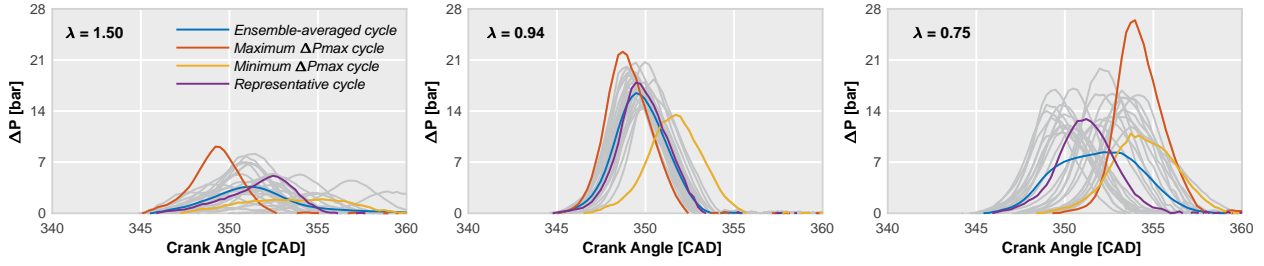


Figure 9: Experimental pressure difference ΔP for individual cycles and $\lambda = 0.94, 1.5$ and 0.75 . Four cycles have been plotted in a different colour, namely the sample mean case, those with the maximum and minimum peak of ΔP and the representative cycle, which has been obtained as described in the text.

362 Our previous analysis has shown that a range of pressure traces ranging from a maximum to a minimum pressure difference between the pre-chamber and main-chamber are obtained. Aside from the
 363 ensemble-averaged mean cycle, an experimental cycle, chosen based on a merit function is considered
 364 as a good representation of a typical cycle. This section evaluates the variability of the predicted jet tip
 365 penetration by feeding these different cycles into the modeling workflow as varying inputs.
 366

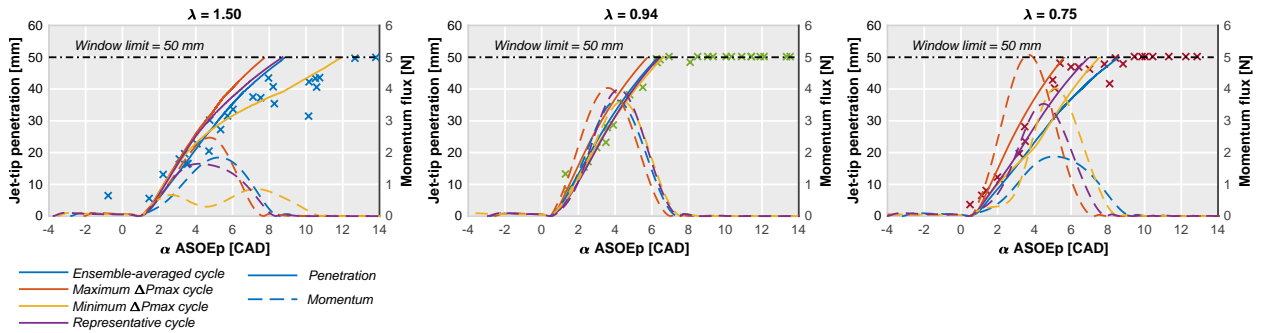


Figure 10: Comparison of jet tip penetration values calculated based on IR images (single markers) with 1-D gas jet simulation results (colored lines). Simulated jet momentum profiles for the four different input cycles (dashed lines) are also shown. Crank angle values are referenced to the start of ejection SOE_p based on ΔP threshold exceeding 0.5 bar.

367 Figure 10 compares the simulated jet tip penetration for each of the four characteristic cycles high-
 368 lighted in Figure 9 with the experimental IR-based penetration values, which indicate the tip of the
 369 ejected pre-chamber jets. Input momentum fluxes are also included to bridge the link to orifice condi-
 370 tions. The time scale in Figure 10 is referenced to the start of ejection (SOE_p), as this has proven to be a
 371 more meaningful way of analyzing the experimental results to shed light on the average behavior of the
 372 gas jet independent of its cyclic variability, as discussed in the previous sections. However, it should be

373 noted that this start of ejection (SOE_p) time-referencing removes the timing variations in combustion
374 and only considers intensity differences in combustion development for comparison, but the limited
375 temporal resolution of the IR images do not allow for resolving this information on a cycle-to-cycle
376 basis anyways.

377 The spread (dispersion) in the simulated jet tip penetration values among the different cycles is
378 similar to the observed experimental trend, i.e., the overall prediction is more accurate for stoichiomet-
379 ric and rich cases. The spread is minimum for the stoichiometric condition and especially high for the
380 lean case. If this variation is quantified in terms of jet tip penetration reaching 50 mm (the limit of the
381 visualization window), it is clear that for the stoichiometric case all cycles reach this value of jet tip
382 penetration within 0.5 CAD of each other. However, this interval widens to 3.0 CAD and 4.0 CAD for
383 the rich and lean cases respectively. In addition to this spread, the predicted jet tip penetration shows
384 good agreement with the experimental values for the ensemble-averaged cycle only under stoichiomet-
385 ric conditions. For the rich and lean conditions, as the pressure difference (and as a consequence the
386 input heat-release rate) evolution of the ensemble-averaged cycle is much flatter and wider than most
387 of the cycles (c.f. Figure 9), there is a reduced momentum flux leading to less accurate jet tip penetra-
388 tion prediction results. Again under extreme conditions such as the rich case ($\lambda = 0.75$), the predicted
389 jet tip penetration for the ensemble-averaged cycle is slower than that of the minimum ΔP_{max} cycle,
390 which is in good agreement with the analysis presented in Figure 9.

391 On the other hand, the predicted jet tip penetration evolution for the representative case is in good
392 agreement with the IR-based penetration values for stoichiometric and rich conditions, with the pre-
393 dicted values typically falling between cycles with minimum and maximum ΔP_{max} . However, for the
394 lean case, the agreement is not so good with experimental cycle-to-cycle variations strongly indicating
395 that accurate predictions on a single-cycle basis become increasing difficult due to combustion instabil-
396 ity at such lean conditions.

397 4.3. Hole-to-hole variation

398 In the previous analysis, the image-based start of ejection values have been averaged over all eight
399 of the pre-chamber orifices, however, high-speed VIS images can also be used to discern the jet-to-jet
400 dispersion between pre-chamber jets emanating from different orifices within a single cycle. Low speed
401 acquisition prevents from using IR images for this purposes. Figure 11 compares the time taken to
402 reach the 5 mm VIS penetration threshold (SOE_{VIS}) for each individual orifice to the orifice-averaged

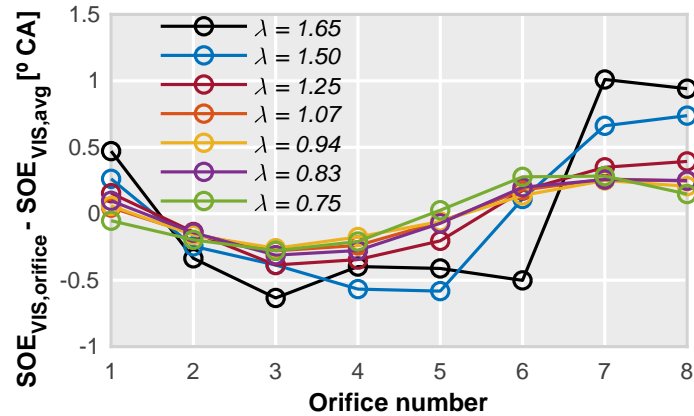


Figure 11: Average deviation of the orifice-resolved start of ejection based on VIS images compared to the sample average one.

403 SOE_{VIS} value (both ensemble-averaged over 30 cycles). Negative and positive values for this deviation
 404 parameter indicate earlier and later start of ejection respectively for a particular orifice when compared
 405 to the orifice-averaged value. In general Figure 11 shows that a clear gas jet ejection pattern exists
 406 in azimuthal direction around the pre-chamber axis, with orifices #2 through #5 ejecting earlier than
 407 the average (based on images such as those in Figure 2, orifice #2 corresponds to the 3 o'clock loca-
 408 tion and the subsequent ones are sequentially numbered in anti-clockwise direction). This sequence is
 409 independent of λ and is most likely caused by the asymmetry existing inside the pre-chamber due to
 410 the location of the spark plug and the injector, which results in a preferential direction for pre-chamber
 411 flame propagation towards the faster orifices (#2 - #5). The maximum and minimum dispersion of this
 412 deviation parameter around the zero value for a given λ indicate the strength of this variation, with
 413 results consistently closer to zero and maximum observable dispersion under stoichiometric and lean
 414 conditions respectively. Such jet-to-jet dispersion in the pre-chamber gas jet ejection is discussed only
 415 in [24], where it is mainly attributed to the asymmetries (non-uniformities) in formation of the ini-
 416 tial spark-kernel inside the pre-chamber. Some of the potential factors that contribute to cycle-to-cycle
 417 and jet-to-jet dispersion in pre-chamber gas jet ejection are spark kernel repeatability, fuel-air mixture
 418 stratification and / or turbulence inside the pre-chamber. However, since no optical access into the
 419 pre-chamber is currently available, one cannot fully discern the true reasons for this behavior using the
 420 current engine configuration.

421 **5. Analysis of events during pre-chamber gas jet ejection**

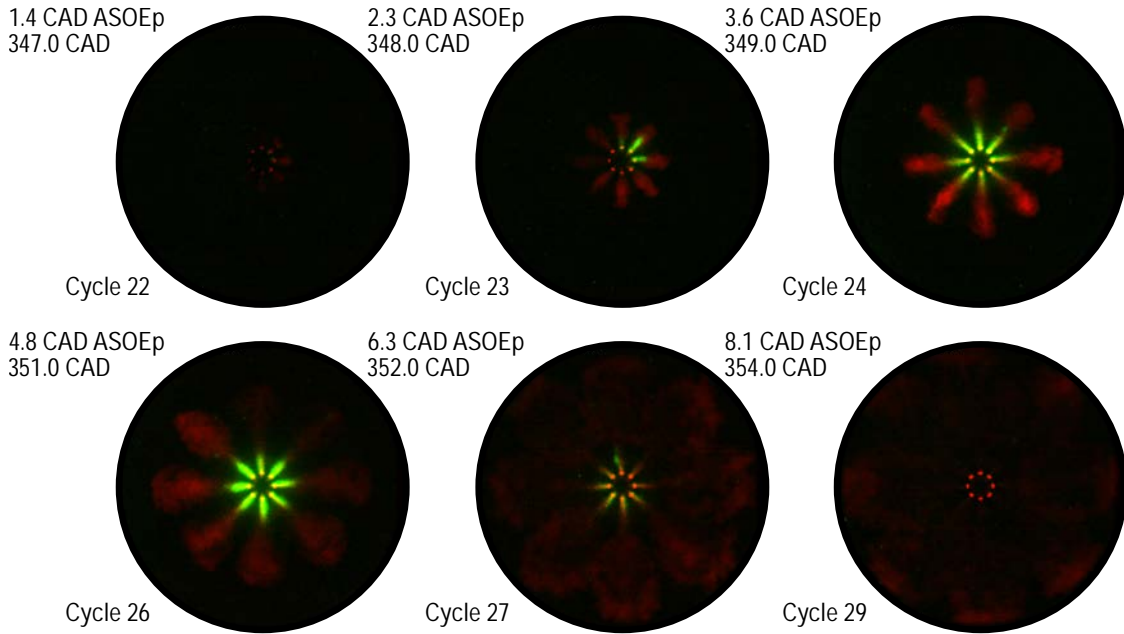


Figure 12: Composite snapshots consisting of simultaneous IR images (red) overlaid on VIS images (green) showing the sequence of events in pre-chamber gas jet ejection for $\lambda = 0.94$. Acquisition CAD (both in absolute terms and after start of ejection ($ASOE_p$) based on ΔP threshold exceeding 0.5 bar) and acquisition cycle number are indicated on the to-left and bottom-left corner of each image.

422 Figure 12 shows a representative sequence of composite snapshots for $\lambda = 0.94$, created by super-
 423 imposing simultaneously acquired IR (employing a red color map) and VIS (employing a green color
 424 map) images. This allows to specifically distinguish between regions of burnt gases (stronger IR emis-
 425 sion from combustion products) and active chemical reactions (stronger chemiluminescence emission
 426 from combustion intermediates) respectively, while describing the overall spatial and temporal evolu-
 427 tion of the pre-chamber jets. Due to the selected color scheme, regions of overlap between IR and VIS
 428 activity appears in shades of yellow. Acquisition CAD for the images is referenced to both absolute
 429 and after start of ejection ($ASOE_p$ defined based on ΔP) based timing based on the individual cycle.
 430 The start of ejection based timing reference results in a steadily increasing IR penetration and a fairly
 431 cycle-independent ΔP , which helps minimize the effect of cycle-to-cycle variations on the analysis to
 432 some extent. Furthermore, the selected operating condition ($\lambda = 0.94$) corresponds to that with the
 433 lowest variation as described earlier.

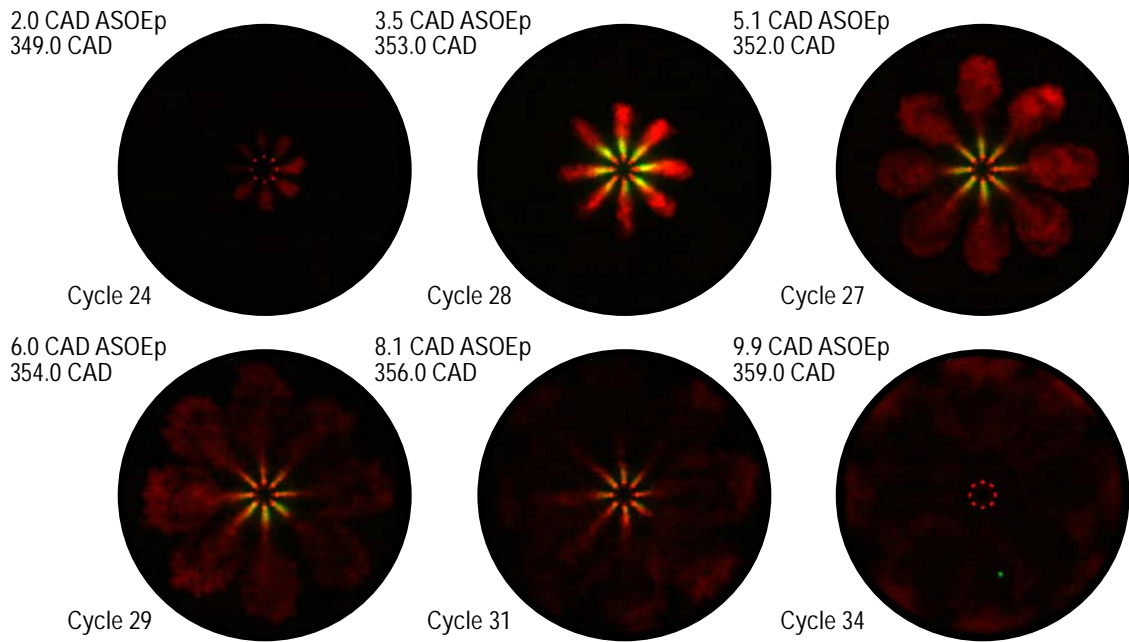


Figure 13: Composite snapshots consisting of simultaneous IR images (red) overlaid on VIS images (green) showing the sequence of events in pre-chamber gas jet ejection for $\lambda = 0.75$. Acquisition CAD (both in absolute terms and after start of ejection (ASOEp) based on ΔP threshold exceeding 0.5 bar) and acquisition cycle number are indicated on the to-left and bottom-left corner of each image.

434 Different events can be observed based upon these images:

- 435 • Ejection of fresh mixture: The first composite snapshot at 1.4 CAD ASOEp shows a preliminary
 436 ejection of mass from the pre-chamber. Since only IR signal is observable without any signs of
 437 broadband chemiluminescence (only shades of red with no shades of green or yellow), it is most
 438 likely that this stems from fresh fuel-air mixture being ejected from the pre-chamber before the
 439 premixed flame-front reaches the orifice.
- 440 • Start of ejection of active products: The second snapshot at 2.3 CAD ASOEp (roughly coinciding
 441 with VIS-based start of ejection) shows the first appearance of broadband chemiluminescence
 442 i.e., pre-chamber gas jet ejection is discernible from VIS images by means of radiation (greenish
 443 regions) in the near-nozzle region, which suggests pre-chamber combustion products reaching
 444 the corresponding orifice. As described earlier, there is a clear asymmetry in the initial VIS pen-
 445 etration, with the 3 o'clock and the adjacent jet in the anti-clockwise direction (#2 and #3 re-
 446 spectively) already penetrating until roughly 10 mm, while no luminosity is observable in other

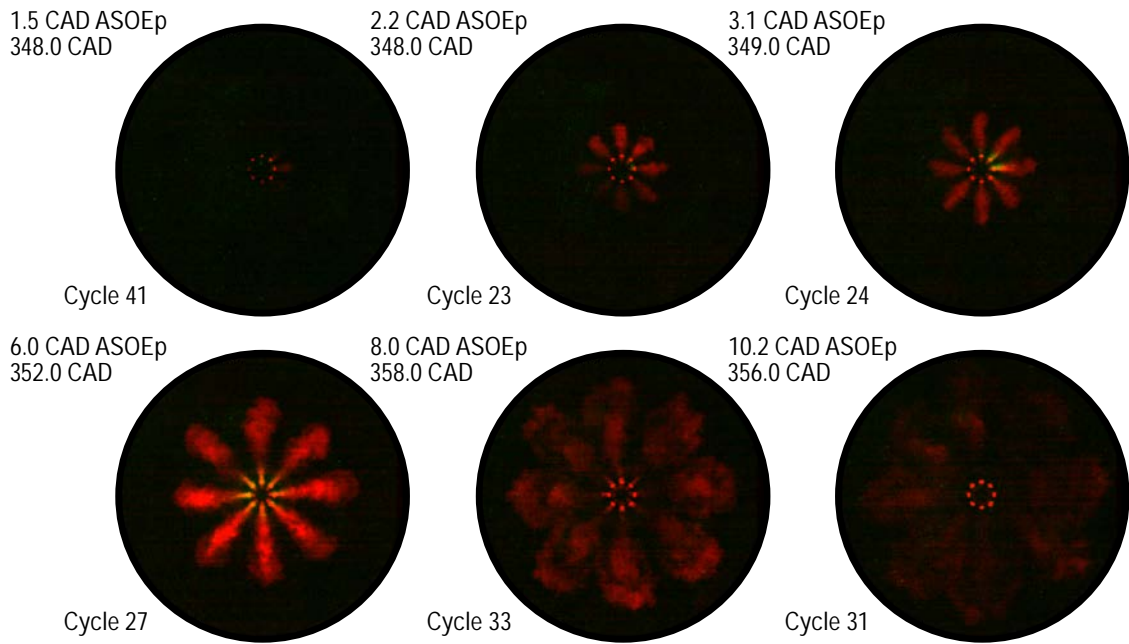


Figure 14: Composite snapshots consisting of simultaneous IR images (red) overlaid on VIS images (green) showing the sequence of events in pre-chamber gas jet ejection for $\lambda = 1.50$. Acquisition CAD (both in absolute terms and after start of ejection ($ASOE_p$) based on ΔP threshold exceeding 0.5 bar) and acquisition cycle number are indicated on the to-left and bottom-left corner of each image.

447 orifices. The IR signal extends further away from the pre-chamber nozzles indicating that the ini-
 448 tially ejected fuel-air mixture reaches deep into the main-chamber. The corresponding IR-based
 449 jet tip penetration is significantly longer than the VIS-based value, with a much more symmetrical
 450 layout. The observed symmetry in the IR imaging confirms that the IR jets initially correspond to
 451 fresh unreacted fuel-air mixture being forced through the pre-chamber orifices, which is mainly
 452 governed by the pressure difference P , thereby resulting in minimal jet-to-jet variation,

- 453 • Peak pressure increase: The third composite snapshot at 3.6 CAD $ASOE_p$ corresponds to the
 454 timing of maximum VIS penetration and roughly maximum ΔP_{max} between the pre-chamber and
 455 main-chamber. The overall appearance of the pre-chamber jets is fairly similar to the previous
 456 snapshot, but with IR signal penetration progressing further into the main-chamber. The main
 457 difference between the two snapshots is in the near-orifice region, where VIS luminosity is almost
 458 symmetrical extending from the eight pre-chamber orifices. The axial extent of the VIS region

459 at this instant is around 11 *mm* and is consistent for all pre-chamber orifices. This potentially
460 indicates that conditions upstream of the orifices are similar, i.e., the premixed flame-front has
461 most likely consumed all the available fuel-air mixture in pre-chamber.

- 462 • Piston window impingement: The fourth composite snapshot at 4.8 *CAD* $ASOE_p$ corresponds to
463 around 1 *CAD* after maximum pressure difference (ΔP_{max}) for that particular cycle is attained.
464 This indicates that the combustion in the pre-chamber is receding, i.e., heat-release cannot com-
465 pensate for the ejection of gas and heat transfer to the surroundings leading to decreasing ΔP .
466 Again, a similar overall pre-chamber gas jet structure is observable based on the IR and VIS im-
467 ages, with a very intense VIS radiation. However, the IR radiation at the jet tip appears wider
468 when compared to the earlier snapshots. As no IR luminosity change is observable in this region,
469 no additional heat-release is to be expected, i.e., there is no evidence of the initially unreacted
470 fuel-air mixture igniting and undergoing combustion. Hence, this widening of the pre-chamber
471 gas jet head cannot be due to combustion, as in a diesel-jet after ignition [44]. Instead, this radial
472 widening of the jet tip appears to be consistent with the gas jet impinging on the piston window,
473 which is confirmed by comparing the IR-based jet tip penetration with the position of the bowl
474 window at that timing.
- 475 • End of ejection: The last two composite snapshots at 6.3 and 8.1 *CAD* $ASOE_p$ correspond to later
476 stages when the pressure difference ΔP drops back to zero. The intensity of gas jet radiation
477 in both VIS and IR is significantly lower than the earlier snapshots. This is especially evident in
478 the VIS region, where radiation primarily stems from chemically reacting products being ejected
479 through the nozzle orifices, which are depleted by the end of pre-chamber combustion process.
480 VIS radiation eventually disappears, while the IR signal extends further in the form a wall gas jet
481 along the piston window towards the cylinder wall. The jet structure essentially vanishes in the
482 last snapshot, where the injected mass appears to be spread across the entire main-chamber. In
483 this particular instant, the radiation at the exit of the pre-chamber orifice is clearly visible, which
484 is most likely caused by thermal radiation emanating from the hot mass remaining within the
485 pre-chamber and / or hot surfaces inside the pre-chamber.

486 Figure 13 and 14 show similar sequence of composite snapshots for a rich ($\lambda = 0.75$) and lean ($\lambda =$
487 1.50) condition respectively. The rich case appears fairly similar to the stoichiometric one discussed
488 earlier in terms of the sequence of events, observed gas jet radiation structure and spatial evolution

489 of the pre-chamber gas jets during the ejection process. Note that in the rich case, it is reasonable to
490 expect some chemical activity extending in the downstream direction, due to the excess fuel in the pre-
491 chamber possibly being oxidized by the air in the main-chamber. However, the IR images do not show
492 any indication of strong radiation at the jet tip, which would possibly indicate local heat release and
493 subsequent temperature rise. The 1-D gas jet model will be used to show that as the gas jet penetrates
494 further downstream of the nozzle, the increasing air entrainment strongly dilutes the ejected mass to
495 mixtures that are too lean to support combustion. This suggests that ambient entrainment plays a
496 leading role in the evolution of the ejected combustion products.

497 As for the lean case, the sequence of events remains consistent but with much lower VIS radiation
498 levels due to the less intense heat release associated with lean combustion. The ejected combustion
499 products from a lean mixture will be significantly different in composition when compared to the other
500 two cases. Furthermore, the lower pressure difference results in lower gas jet momentum at the nozzle
501 leading to a shorter penetration of the gas jet, as modeling will confirm.

502 *5.1. 1-D Modeling analysis of the gas jet ejection process*

503 Figure 15 summarizes 1-D modeling results of jet tip penetration for all operating conditions in
504 this study. Only 1-D model predictions based upon the representative cycle are shown with predicted
505 jet tip penetration values compared to experimental IR- and VIS-based results. The IR-based jet tip
506 penetration values are plotted for all 30 cycles, while only the representative cycle is included for the
507 VIS-based information. Starting with the leanest case, the trends clearly show that IR-based jet tip
508 penetration becomes faster with richer pre-chamber conditions down to $\lambda = 0.94$. The remaining rich
509 cases show very similar jet tip penetration results though the peak momentum slightly decreases, which
510 is in good agreement with the measured peak ΔP values shown in Figure 8.

511 The agreement of the predicted 1-D modeling based jet tip penetration values with the IR-based
512 results is good starting from $\lambda = 1.25$ and into the richer conditions. For the leanest of the conditions,
513 accuracy is just fair. An almost 1 CAD shift between the initial timing of the penetration based on
514 the modeling and experimental results is also observable with the three leanest cases. For these cases,
515 the spread in experimental data is evident, which indicates that combustion is more unstable not just
516 in timing but also in development, hence generating reliable modeling predictions becomes far more
517 difficult. For the other stoichiometric and rich conditions, the agreement between the modeling and
518 experimental results is quite remarkable.

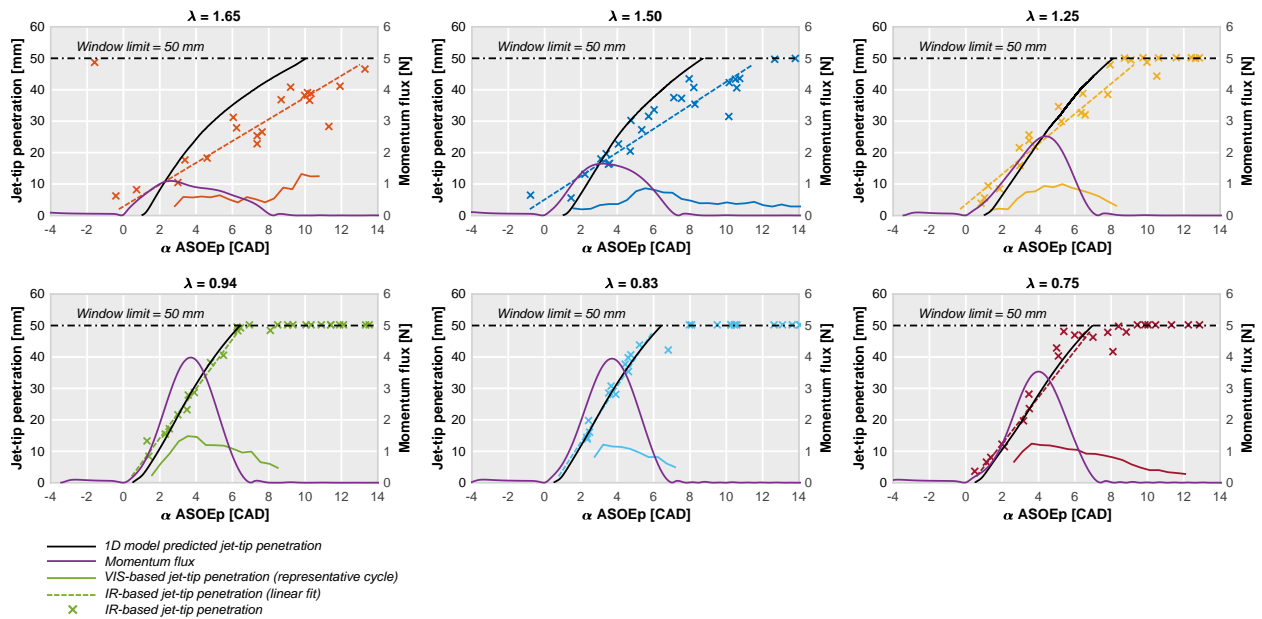


Figure 15: Comparison of jet tip penetration based on IR (single markers - all cycles, dotted line - linear fit) and VIS (colored line - only representative cycle) imaging with predicted jet tip penetration values (black line) using the input data from the representative cycle. Momentum flux used for the simulation is also included. Crank angle values are referenced to the start of ejection SOE_p based on ΔP exceeding 0.5 bar.

519 Figure 16 provides further insight into the evolution of flow dynamics along the gas jet axis during
 520 the ejection process for $\lambda = 0.94$ using the representative engine cycle. Corresponding momentum
 521 flux at the nozzle and the modeled gas jet tip penetration have been presented earlier in Figure 10.
 522 Mass and momentum fluxes along the gas jet axial coordinate at different instances during the ejection
 523 process are shown with colors signifying the crank angle timing. To facilitate analysis, plots are split into
 524 two intervals corresponding to timings before and after the occurrence of maximum momentum flux.
 525 During the initial stage of the ejection process (left plots in Figure 16), both momentum flux and mass
 526 flow increase with time as expected. A gas jet can be considered as a set of momentum flux parcels that
 527 travel downstream incorporating ('entraining') ambient gas, which is quantified in terms of the mass
 528 flux. At any given instant, the momentum flux decreases with the axial distance as the parcels with the
 529 highest momentum are the latest injected ones, which are much closer to the orifice. Such parcels tend
 530 to push the ones ahead thereby transferring momentum towards the jet tip. On the other hand, mass
 531 flux at any given instant is always increasing with axial distance as the entrainment of ambient mass

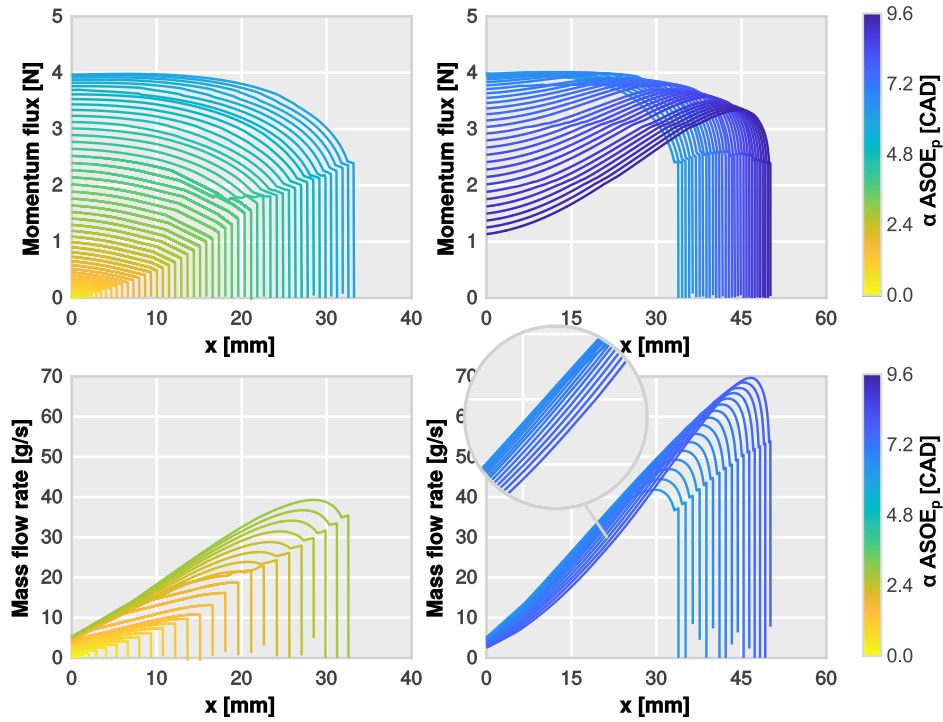


Figure 16: Spatial distribution of momentum (top) and mass fluxes (bottom) along the axial coordinate of the gas jet at different instances during pre-chamber gas jet ejection process for $\lambda = 0.94$ using the representative cycle. Colored contours correspond to different timings indicated by CAD values after SOE_p as shown by the color bar. Plots on the left correspond to timings between start of ejection and the occurrence of maximum momentum flux, while plots on the right correspond to subsequent timings until the end of ejection.

532 from the main-chamber starts at the nozzle and increases with the parcel timeline, i.e. along the axial
 533 distance. This means that the ejected pre-chamber gas jet flow becomes increasingly diluted with axial
 534 distance.

535 Consistent with the previous description of the gas jet, the later ejected parcels (right plots in Fig-
 536 ure 16) have lower momentum than the ones ejected earlier. Hence, starting from the earlier slightly
 537 decreasing axial distribution, the shape of the momentum flux progressively turns into an increasing
 538 function. This means that the newly injected parcels do not help in pushing the jet tip anymore. As for
 539 the mass flux, the axially-increasing trend remains the same during the second phase, as ambient mass
 540 is steadily being incorporated into the spray due to the momentum flux. However, mass flux values at
 541 a given axial position steadily decrease with time, although the temporal decrease rate is much lower

542 than that of the momentum flux. This evolution is similar to the end of injection event in diesel-like
 543 sprays, investigated in detail in [34]. Owing to the decreasing momentum flux, progress in jet tip pene-
 544 tration in the second phase is roughly only 15 mm compared to the initial increase of more than 30 mm
 545 during the first phase of the pre-chamber gas jet ejection process.

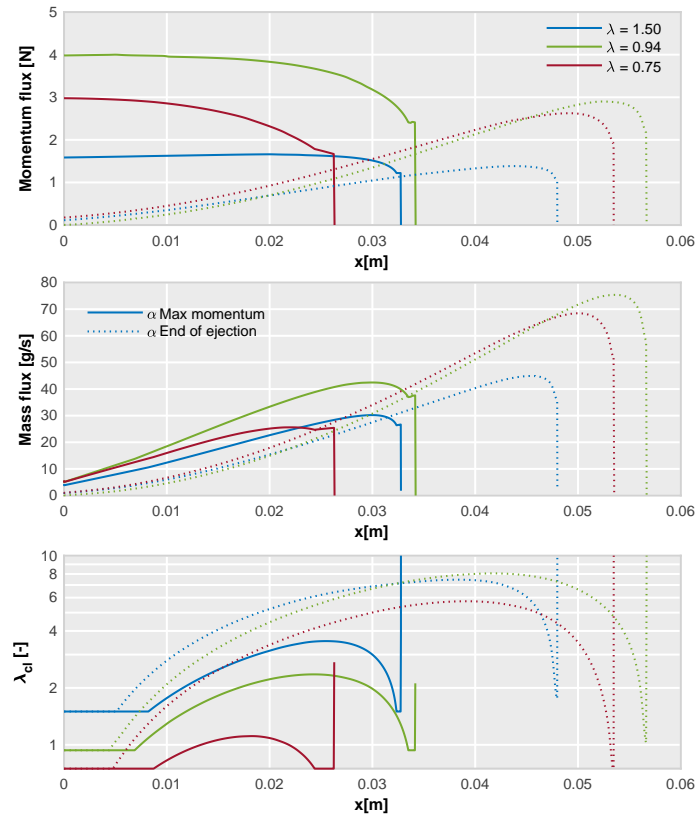


Figure 17: Spatial distribution of momentum (top) and mass fluxes (middle), as well as air-excess ratio λ_{cl} (bottom) along the axial coordinate of the gas jet for $\lambda = 1.55, 0.94$ and 0.75 using the representative cycle. Timings correspond to the instance of maximum momentum flux (solid line) and the end of ejection (dashed line).

546 Figure 17 compares the magnitudes of mass and momentum fluxes for three operating conditions,
 547 namely $\lambda = 1.55, 0.94$ and 0.75 at two characteristic timings, namely during the occurrence of peak
 548 momentum flux at the orifice (last timing on Figure 16, left) and at the end of ejection (last timing
 549 on Figure 16, right). The previously observed trends for momentum and mass flux distribution along
 550 the spray axis remain relatively similar for all three operating conditions at both timings. During the
 551 maximum momentum flux timing at the orifice, the results clearly indicate higher local momentum and

552 mass fluxes for the stoichiometric condition compared to the other conditions, due to the more rapid
553 pre-chamber combustion development. A higher momentum flux leads to more intense entrainment of
554 ambient air and hence increased mass flow.

555 Entrainment effects are also estimated in terms of a third variable shown on the plot, namely the
556 air-fuel ratio λ_{cl} along the gas jet axis. This will be the richest location within the jet cross-section at
557 each axial position of the gas jet, as the fuel mass fraction profiles are assumed to follow a Gaussian
558 distribution in the 1-D model. In the near-orifice region, the local value of λ_{cl} correlates to the cor-
559 responding pre-chamber λ value, and increases after remaining constant for a short distance. Beyond
560 this region, the stoichiometric pre-chamber condition exhibits the most prominent increase in λ_{cl} up to
561 around 15 mm, indicating faster entrainment; despite this, it never reaches λ_{cl} values associated with
562 the leanest condition. Furthermore, none of the three shown λ_{cl} evolution intersect with each other.
563 The decreasing trend observed at the tip of the jet is an artifact of the 1D simplification of the jet tip
564 zone, which is specially evident for highly transient injection velocity, as already shown in [36].

565 At the end of ejection timing, results show that the spray tip propagates with larger momentum for
566 the stoichiometric condition compared to the other two. However, distribution of mass and momentum
567 fluxes remain fairly similar for all three conditions starting from the orifice exit up to around 30 mm
568 downstream. This indicates that the second phase of gas jet ejection (following the occurrence of peak
569 momentum flux) results in a very similar flow state near the vicinity of the pre-chamber orifice at the
570 end of the ejection process. In other words, the initial ramp-up period of ejection until the occurrence
571 of maximum momentum flux is the most dependent on pre-chamber combustion characteristics. For
572 scenarios with fuel-air mixtures present in the main-chamber, the subsequent combustion development
573 is most likely to be influenced by this initial ejection phase, as the ramp-down phase of ejection collapses
574 to very similar flow distributions, almost independent of the operating conditions.

575 Information derived from the 1-D model analysis also provides a rough quantification for the dilu-
576 tion of the ejected pre-chamber gases. As seen from the experimental images, there is no evidence of
577 chemical activity in regions situated further downstream of the maximum VIS penetration length (8 to
578 15 mm depending on λ). According to the estimations of the 1-D model, the richest locations within
579 the gas jet at the timing of maximum momentum flux will all be below a local $\lambda = 2$ for distances
580 longer than 15 mm, except for the stoichiometric case. At the end of ejection timing, the plot shows all
581 conditions being much leaner than the $\lambda = 2$. Keeping in mind that most of the ejected mass will be

582 leaner than the values shown on the spray axis, the resulting mixture is most likely too lean to react,
583 which is in agreement with the absence of chemical activity in the experimental images downstream of
584 the maximum VIS penetration.

585 **6. Summary and conclusions**

586 This work reports an experimental study of pre-chamber gas jets ejected into the main-chamber
587 (air ambient) in a heavy-duty, single-cylinder optical engine. This pre-chamber only fueling strategy
588 eliminates the effect of ignition and subsequent combustion development in the main-chamber on pre-
589 chamber gas jet flow dynamics. Different objectives have been achieved, namely the detailed description
590 of the near-orifice hot jets structure by means of high-speed visible imaging, the quantification of the
591 tip penetration by means of low speed infrared imaging, a detailed analysis of cycle-to-cycle scattering
592 as well as the validation of a 1-D gas jet model to describe the ejected gas flow dynamics.

593 The main conclusions of this study are summarized as follows:

- 594 • Cycle-to-cycle variation in the ejection process is quantified in detail in terms of both pressure
595 difference and jet-penetration. As expected, stable combustion is achieved around stoichiometric
596 conditions due to rapid heat-release.
- 597 • Although cycle-to-cycle variations are linked to maximum burning rate and thereby to the peak
598 pressure in the pre-chamber, most of the observed fluctuations tend to disappear when refer-
599 encing the time evolution to the start of ejection, which is defined based on a threshold pres-
600 sure difference of 0.5 *bar* or a visible radiation penetration threshold of 5 *mm*. Thus, most of
601 the fluctuations are related to the start of combustion in the pre-chamber. Jet-to-jet variations
602 shows a repeatable ignition sequence with some orifices ejecting earlier than others do. This most
603 likely stems from the differences in the dynamics of premixed flame-front propagation within the
604 pre-chamber. This is most likely due to the intense turbulence induced stratification of the pre-
605 chamber charge caused by the fuel injection event and the stochastic nature of ignition event, but
606 further investigation is warranted to confirm this hypothesis.
- 607 • Combustion evolution is described using visible and infrared images. Ejection of unreacted fresh
608 fuel-air mixture into the main-chamber is detected from infrared images initially due to the fa-
609 vorable pressure drop across the orifice. Visible radiation is detected only after a delay (typically

610 in the order of 2.5 *CAD*) from the start of ejection as defined in terms of pressure difference
611 (ΔP). This chemiluminescence activity is limited exclusively to the vicinity of the orifice, while
612 downstream of this region only infrared radiation is observable. No indication of chemical ac-
613 tivity is detectable in the infrared-only region, which is most likely due to the ultra-lean mixture
614 composition (no fueling of the main-chamber).

- 615 • A 1-D spray model is adapted to predict tip-penetration of ejected pre-chamber gas jets. Flow
616 conditions at the orifice (mass and momentum fluxes) are obtained using a 0-D analysis of the
617 pre-chamber and main chamber. Time-varying ambient conditions in the pre-chamber are also
618 obtained from the 0-D analysis.
- 619 • Variation in the tip-penetration is quantified based on 1-D model predictions with different input
620 data derived from corresponding experimental runs. Conditions of sample mean pressure rise
621 along with extreme values (maximum and minimum) of pressure increase are evaluated along
622 with a *representative cycle*, selected based on a merit function. The representative cycle case pro-
623 vides most accurate predictions of tip-penetration, while the sample mean case performs poorly
624 especially in conditions with significant cycle-to-cycle variation. Hence, the proposed 1-D com-
625 putational tool can be used for pre-chamber gas jet tip-penetration predictions with reasonable
626 certainty.
- 627 • Analysis of the 1-D jet model predictions suggests that the initial ejection process, i.e., until the
628 point of maximum momentum flux at the nozzle, is highly dependent on the air-fuel ratio λ in the
629 pre-chamber. Hence, the local flow and most likely the associated combustion development for
630 fuelled main-chamber scenario will be highly dependent on this early-ejection phase. Flow evolu-
631 tion at later timings becomes relatively independent of λ in the pre-chamber, with a characteristic
632 fast slow-down due to the steeply decreasing ejection velocities.

633 **Acknowledgements**

634 This research was sponsored by the U.S. Department of Energy (DOE) Office of Energy Efficiency and
635 Renewable Energy (EERE). Optical engine experiments were conducted at the Combustion Research
636 Facility, Sandia National Laboratories, Livermore, CA. Sandia National Laboratories is a multi-mission

637 laboratory managed and operated by National Technology and Engineering Solutions of Sandia, LLC., a
638 wholly owned subsidiary of Honeywell International, Inc., for the U.S. Department of Energy's National
639 Nuclear Security Administration under contract DE-NA0003525.

640 José M García-Oliver acknowledges the support of the Generalitat Valenciana government in Spain
641 through Grant Best/2019/176 for his scientific visit to the Combustion Research Facility. P. J. Martínez-
642 Hernández is partly supported by an FPI contract (FPI-S2-19-21993) of the “Programa de Apoyo para
643 la Investigación y Desarrollo (PAID-05-19)” of the Universitat Politècnica de València.

644 References

- 645 [1] S. Heyne, M. Meier, B. Imbert, D. Favrat, Experimental investigation of prechamber autoignition in a natural gas engine
646 for cogeneration, *Fuel* 88 (3) (2009) 547 – 552. doi:<https://doi.org/10.1016/j.fuel.2008.09.032>.
- 647 [2] A. Jamrozik, Lean combustion by a pre-chamber charge stratification in a stationary spark ignited engine, *Journal of*
648 *Mechanical Science and Technology* 29 (5) (2015) 2269–2278. doi:<https://doi.org/10.1007/s12206-015-0145-7>.
- 649 [3] J. Benajes, R. Novella, J. Gomez-Soriano, I. Barbery, C. Libert, F. Rampanarivo, M. Dabiri, Computational assessment to-
650 wards understanding the energy conversion and combustion process of lean mixtures in passive pre-chamber ignited en-
651 gines, *Applied Thermal Engineering* 178 (2020) 115501. doi:[https://doi.org/10.1016/j.applthermaleng.2020.](https://doi.org/10.1016/j.applthermaleng.2020.115501)
652 [115501](https://doi.org/10.1016/j.applthermaleng.2020.115501).
- 653 [4] P. Hlaing, M. Echeverri Marquez, E. Singh, F. Almatrafi, E. Cenker, M. Ben Houidi, B. Johansson, Effect of pre-chamber
654 enrichment on lean burn pre-chamber spark ignition combustion concept with a narrow-throat geometry, *WCX SAE*
655 *World Congress Experience 2020-01-0825* (2020). doi:[10.4271/2020-01-0825](https://doi.org/10.4271/2020-01-0825).
- 656 [5] A. Shah, Improving the efficiency of gas engines using pre-chamber ignition, Ph.D. thesis, Lund University (2015).
- 657 [6] E. Toulson, H. J. Schock, W. P. Attard, A review of pre-chamber initiated jet ignition combustion systems, *SAE 2010*
658 *Powertrains Fuels & Lubricants Meeting 2010-01-2263* (2010). doi:<https://doi.org/10.4271/2010-01-2263>.
- 659 [7] A. Shah, P. Tunestal, B. Johansson, Effect of relative mixture strength on performance of divided chamber ‘avalanche
660 activated combustion’ ignition technique in a heavy duty natural gas engine, *SAE 2014 World Congress & Exhibition*
661 *2014-01-1327* (2014). doi:<https://doi.org/10.4271/2014-01-1327>.
- 662 [8] W. P. Attard, M. Bassett, P. Parsons, H. Blaxill, A new combustion system achieving high drive cycle fuel econ-
663 omy improvements in a modern vehicle powertrain, *SAE 2011 World Congress & Exhibition 2011-01-0664* (2011).
664 doi:<https://doi.org/10.4271/2011-01-0664>.
- 665 [9] J. Pan, Z. Hu, H. Wei, M. Pan, X. Liang, G. Shu, L. Zhou, Understanding strong knocking mechanism through high-
666 strength optical rapid compression machines, *Combustion and Flame* 202 (2019) 1–15. doi:[https://doi.org/10.](https://doi.org/10.1016/j.combustflame.2019.01.004)
667 [1016/j.combustflame.2019.01.004](https://doi.org/10.1016/j.combustflame.2019.01.004).
- 668 [10] C. Chen, P. Pal, M. Ameen, D. Feng, H. Wei, Large-eddy simulation study on cycle-to-cycle variation of knocking com-
669 bustion in a spark-ignition engine, *Applied Energy* 261 (2020) 114447. doi:[https://doi.org/10.1016/j.apenergy.](https://doi.org/10.1016/j.apenergy.2019.114447)
670 [2019.114447](https://doi.org/10.1016/j.apenergy.2019.114447).

- 671 [11] A. Broatch, R. Novella, J. García-Tíscar, J. Gomez-Soriano, P. Pal, Investigation of the effects of turbulence modeling
672 on the prediction of compression-ignition combustion unsteadiness, *International Journal of Engine Research* (2021)
673 1468087421990478.
- 674 [12] W. P. Attard, H. Blaxill, A gasoline fueled pre-chamber jet ignition combustion system at unthrottled conditions, *SAE*
675 *International Journal of Engines* 5 (2) (2012) 315–329. doi:<https://doi.org/10.4271/2012-01-0386>.
- 676 [13] C. E. C. Alvarez, G. E. Couto, V. R. Roso, A. B. Thiriet, R. M. Valle, A review of prechamber ignition systems as lean
677 combustion technology for si engines, *Applied Thermal Engineering* 128 (2018) 107 – 120. doi:[https://doi.org/](https://doi.org/10.1016/j.applthermaleng.2017.08.118)
678 [10.1016/j.applthermaleng.2017.08.118](https://doi.org/10.1016/j.applthermaleng.2017.08.118).
- 679 [14] Natural gas vehicle research workshop, U.S. Department of Energy - Vehicle Technologies Office, 2017.
- 680 [15] S. Yamaguchi, N. Ohiwa, T. Hasegawa, Ignition and burning process in a divided chamber bomb, *Combustion and Flame*
681 59 (2) (1985) 177 – 187. doi:[https://doi.org/10.1016/0010-2180\(85\)90023-9](https://doi.org/10.1016/0010-2180(85)90023-9).
- 682 [16] S. Biswas, S. Tanvir, H. Wang, L. Qiao, On ignition mechanisms of premixed ch₄/air and h₂/air using a hot turbulent jet
683 generated by pre-chamber combustion, *Applied Thermal Engineering* 106 (2016) 925 – 937. doi:[https://doi.org/](https://doi.org/10.1016/j.applthermaleng.2016.06.070)
684 [10.1016/j.applthermaleng.2016.06.070](https://doi.org/10.1016/j.applthermaleng.2016.06.070).
- 685 [17] S. Biswas, L. Qiao, Ignition of ultra-lean premixed hydrogen/air by an impinging hot jet, *Applied energy* 228 (2018)
686 954–964. doi:<https://doi.org/10.1016/j.apenergy.2018.06.102>.
- 687 [18] E. Mastorakos, P. Allison, A. Giusti, P. De Oliveira, S. Benekos, Y. Wright, C. Frouzakis, K. Boulouchos, Fundamental
688 aspects of jet ignition for natural gas engines, *SAE International Journal of Engines* 5 (10) (2017) 2429–2438. doi:
689 <https://doi.org/10.4271/2017-24-0097>.
- 690 [19] P. Allison, M. de Oliveira, A. Giusti, E. Mastorakos, Pre-chamber ignition mechanism: Experiments and simulations on
691 turbulent jet flame structure, *Fuel* 230 (2018) 274–281. doi:[10.1016/j.fuel.2018.05.005](https://doi.org/10.1016/j.fuel.2018.05.005).
- 692 [20] G. Gentz, B. Thelen, P. Litke, J. Hoke, E. Toulson, Combustion visualization, performance, and cfd modeling of a pre-
693 chamber turbulent jet ignition system in a rapid compression machine, *SAE International Journal of Engines* 8 (2)
694 (2015) 538–546. doi:<https://doi.org/10.4271/2015-01-0779>.
- 695 [21] M. Gholamisheeri, B. C. Thelen, G. R. Gentz, I. S. Wichman, E. Toulson, Rapid compression machine study of a premixed,
696 variable inlet density and flow rate, confined turbulent jet, *Combustion and Flame* 169 (2016) 321 – 332. doi:[https://doi.org/](https://doi.org/10.1016/j.combustflame.2016.05.001)
697 [10.1016/j.combustflame.2016.05.001](https://doi.org/10.1016/j.combustflame.2016.05.001).
- 698 [22] S. Schlatter, B. Schneider, Y. M. Wright, K. Boulouchos, Comparative study of ignition systems for lean burn gas engines
699 in an optically accessible rapid compression expansion machine, *11th International Conference on Engines & Vehicles*
700 2013-24-0112 (2013). doi:<https://doi.org/10.4271/2013-24-0112>.
- 701 [23] J. Benajes, R. Novella, J. Gomez-Soriano, P. Martinez-Hernandez, C. Libert, M. Dabiri, Evaluation of the passive pre-
702 chamber ignition concept for future high compression ratio turbocharged spark-ignition engines, *Applied Energy* 248
703 (2019) 576 – 588. doi:<https://doi.org/10.1016/j.apenergy.2019.04.131>.
- 704 [24] X. Li, W. Zhang, Z. Huang, D. Ju, L. Huang, M. Feng, X. Lu, Z. Huang, Pre-chamber turbulent jet ignition of methane/air
705 mixtures with multiple orifices in a large bore constant volume chamber: effect of air-fuel equivalence ratio and pre-
706 mixed pressure, *Frontiers in Energy* 13 (3) (2019) 483–493. doi:[10.1007/s11708-019-0631-1](https://doi.org/10.1007/s11708-019-0631-1).

- 707 [25] A. Shah, P. Tunestål, B. Johansson, Cfd simulations of pre-chamber jets' mixing characteristics in a heavy duty natural
708 gas engine, JSAE/SAE 2015 International Powertrains, Fuels & Lubricants Meeting 2015-01-1890 (2015). doi:<https://doi.org/10.4271/2015-01-1890>.
709
- 710 [26] G. Kammel, F. Mair, J. Zelenka, M. Lackner, A. Wimmer, G. Kogler, E. Bärow, Simulation based predesign and experimen-
711 tal validation of a prechamber ignited hpdi gas combustion conceptdoi:<https://doi.org/10.4271/2019-01-0259>.
- 712 [27] G. Xu, Y. M. Wright, M. Schiliro, K. Boulouchos, Characterization of combustion in a gas engine ignited using a small
713 un-scavenged pre-chamber, International Journal of Engine Research 21 (7) 1085–1106. doi:<https://doi.org/10.1177/1468087418798918>.
714
- 715 [28] B. Korb, K. Kuppa, H. D. Nguyen, F. Dinkelacker, G. Wachtmeister, Experimental and numerical investigations of charge
716 motion and combustion in lean-burn natural gas engines, Combustion and Flame 212 (2020) 309–322. doi:<https://doi.org/10.1016/j.combustflame.2019.11.005>.
717
- 718 [29] A. Validi, H. Schock, F. Jaber, Turbulent jet ignition assisted combustion in a rapid compression machine, Combustion
719 and Flame 186 (2017) 65–82. doi:<https://doi.org/10.1016/j.combustflame.2017.07.032>.
- 720 [30] Q. Malé, G. Staffelbach, O. Vermorel, A. Misdariis, F. Ravet, T. Poinso, Large eddy simulation of pre-chamber ignition in
721 an internal combustion engine, Flow, Turbulence and Combustion 103 (2) (2019) 465–483. doi:<https://doi.org/10.1007/s10494-019-00026-y>.
722
- 723 [31] A. Validi, F. Jaber, Numerical study of turbulent jet ignition in a lean premixed configuration, Flow, Turbulence and
724 Combustion 100 (1) (2018) 197–224. doi:<https://doi.org/10.1007/s10494-017-9837-7>.
- 725 [32] F. Qin, A. Shah, Z.-w. Huang, L.-n. Peng, P. Tunestal, X.-S. Bai, Detailed numerical simulation of transient mixing and
726 combustion of premixed methane/air mixtures in a pre-chamber/main-chamber system relevant to internal combustion
727 engines, Combustion and Flame 188 (2018) 357–366. doi:<https://doi.org/10.1016/j.combustflame.2017.10.006>.
728
- 729 [33] S. Benekos, C. E. Frouzakis, G. K. Giannakopoulos, M. Bolla, Y. M. Wright, K. Boulouchos, Prechamber ignition: An
730 exploratory 2-d dns study of the effects of initial temperature and main chamber composition, Combustion and Flame
731 215 (2020) 10–27. doi:<https://doi.org/10.1016/j.combustflame.2020.01.014>.
- 732 [34] M. P. B. Musculus, K. Kattke, Entrainment waves in diesel jets, SAE International Journal of Engines 2 (11) 1170–1193.
733 doi:[10.4271/2009-01-1355](https://doi.org/10.4271/2009-01-1355).
- 734 [35] L. M. Pickett, J. Manin, C. L. Genzale, D. L. Siebers, M. P. B. Musculus, C. A. Idicheria, Relationship Between Diesel
735 Fuel Spray Vapor Penetration/Dispersion and Local Fuel Mixture Fraction, SAE International Journal of Engines (1)
736 764–799. doi:[10.4271/2011-01-0686](https://doi.org/10.4271/2011-01-0686).
- 737 [36] J. V. Pastor, J. J. López, J. M. García, J. M. Pastor, A 1d model for the description of mixing-controlled inert diesel sprays,
738 Fuel 87 (13) (2008) 2871 – 2885. doi:<https://doi.org/10.1016/j.fuel.2008.04.017>.
- 739 [37] G. N. Abramovich, The theory of turbulent jets, The MIT Press Classics, 1963.
- 740 [38] K. Bardis, P. Kyratos, G. Xu, C. Barro, Y. M. Wright, K. Boulouchos, Development and validation of a novel quasi-
741 dimensional combustion model for un-scavenged prechamber gas engines with numerical simulations and engine ex-
742 periments, International Journal of Engine Research (2020) 1468087420951338.
- 743 [39] J. Benajes, R. Novella, J. Gomez-Soriano, I. Barbery, C. Libert, Advantages of hydrogen addition in a passive pre-chamber
744 ignited si engine for passenger car applications, International Journal of Energy Research.

- 745 [40] J. O'Connor, M. P. B. Musculus, Effects of exhaust gas recirculation and load on soot in a heavy-duty optical diesel engine
746 with close-coupled post injections for high-efficiency combustion phasing, *International Journal of Engine Research* (4)
747 421–443. doi:10.1177/1468087413488767.
- 748 [41] J. B. Heywood, et al., *Internal combustion engine fundamentals*, McGraw-Hill New York, 1988.
- 749 [42] R. Novella, J. Gomez-Soriano, P. Martinez-Hernandez, C. Libert, F. Rampanarivo, Improving the performance of the
750 passive pre-chamber ignition concept for spark-ignition engines fueled with natural gas, *Fuel* 290 (2021) 119971.
751 doi:https://doi.org/10.1016/j.fuel.2020.119971.
- 752 [43] J. Desantes, J. Pastor, J. García-Oliver, J. Pastor, A 1d model for the description of mixing-controlled reacting diesel
753 sprays, *Combustion and Flame* 156 (1) (2009) 234 – 249. doi:https://doi.org/10.1016/j.combustflame.2008.
754 10.008.
- 755 [44] J. Desantes, J. García-Oliver, T. Xuan, W. Vera-Tudela, A study on tip penetration velocity and radial expansion of reacting
756 diesel sprays with different fuels, *Fuel* 207 (2017) 323 – 335. doi:https://doi.org/10.1016/j.fuel.2017.06.108.
- 757 [45] J. V. Pastor, J. M. Garcia-Oliver, J. M. Pastor, W. Vera-Tudela, One-dimensional diesel spray modeling of multicomponent
758 fuels, *Atomization and Sprays* 25 (6) (2015). doi:10.1615/AtomizSpr.2014010370.
- 759 [46] J. Desantes, R. Payri, F. Salvador, A. Gil, Development and validation of a theoretical model for diesel spray penetration,
760 *Fuel* 85 (2006) 910–917. doi:10.1016/j.fuel.2005.10.023.
- 761 [47] P. Pal, C. Kolodziej, S. Choi, S. Som, A. Broatch, J. Gomez-Soriano, Y. Wu, T. Lu, Y. C. See, Development of a virtual
762 cfr engine model for knocking combustion analysis, *SAE International Journal of Engines* 11 (6) (2018) 1069–1082.
763 doi:https://doi.org/10.4271/2018-01-0187.